Simultaneous proteome localization and turnover analysis reveals spatiotemporal features of protein homeostasis disruptions

[1]Jordan Currie, [1]Vyshnavi Manda, [1]Sean K. Robinson, [4]Celine Lai, [5]Vertica Agnihotri, [1]Veronica Hidalgo, [1]R. W. Ludwig, [6]Kai Zhang, [1]Jay Pavelka, [6]Zhao V. Wang, [5]June-Wha Rhee, [1,2,3]Maggie P. Y. Lam, [1,3]Edward Lau

1. Department of Medicine
2. Department of Biochemistry and Molecular Genetics
3. Consortium for Fibrosis Research and Translation
   University of Colorado School of Medicine
   Aurora, CO 80045, USA
4. Stanford Cardiovascular Institute
   Stanford University
   Stanford, CA 94305, USA
5. Department of Medicine, Division of Cardiology
   City of Hope Comprehensive Cancer Center
   Durante, CA 91010, USA
6. Department of Diabetes and Cancer Metabolism
   Beckman Research Institute, City of Hope National Medical Center
   Duarte, CA 91010, USA

Correspondence
Edward Lau, PhD: edward.lau@cuanschutz.edu

Abstract

The functions of proteins depend on their spatial and temporal distributions, which are not directly measured by static protein abundance. Under endoplasmic reticulum (ER) stress, the unfolded protein response (UPR) pathway remediates proteostasis in part by altering the turnover kinetics and spatial distribution of proteins. A global view of these spatiotemporal changes has yet to emerge and it is unknown how they affect different cellular compartments and pathways. Here we describe a mass spectrometry-based proteomics strategy and data analysis pipeline, termed Simultaneous Proteome Localization and Turnover (SPLAT), to measure concurrently the changes in protein turnover and subcellular distribution in the same experiment. Investigating two common UPR models of thapsigargin and tunicamycin challenge in human AC16 cells, we find that the changes in protein turnover kinetics during UPR varies across subcellular localizations, with overall slowdown but an acceleration in endoplasmic reticulum and Golgi proteins involved in stress response. In parallel, the spatial proteomics component of the experiment revealed an externalization of amino acid transporters and ion channels under UPR, as well as the migration of RNA-binding proteins toward an endosome co-sedimenting compartment. The SPLAT

experimental design classifies heavy and light SILAC labeled proteins separately, allowing the observation of differential localization of new and old protein pools and capturing a partition of newly synthesized EGFR and ITGAV to the ER under stress that suggests protein trafficking disruptions. Finally, application of SPLAT toward human induced pluripotent stem cell derived cardiomyocytes (iPSC-CM) exposed to the cancer drug carfilzomib, identified a selective disruption of proteostasis in sarcomeric proteins as a potential mechanism of carfilzomib-mediated cardiotoxicity. Taken together, this study provides a global view into the spatiotemporal dynamics of human cardiac cells and demonstrates a method for inferring the coordinations between spatial and temporal proteome regulations in stress and drug response.

Keywords

Unfolded protein response, protein turnover, spatial proteomics, mass spectrometry, stress response, subcellular localization, spatiotemporal dynamics

Introduction

Protein turnover is an important cellular process that maintains the quality and quantity of protein pools in homeostasis, and involves fine regulations of the rates of synthesis and degradation of individual proteins. A close relationship exists between turnover kinetics with the spatial distribution of proteins. Cellular organelles including the cytosol, endoplasmic reticulum (ER), and mitochondria are equipped with distinct quality control and proteolytic mechanisms that maintain protein folding and regulate protein degradation in a localization dependent manner (Lemberg and Strisovsky, 2021; Mårtensson et al., 2019; Tsai et al., 2022). Newly synthesized proteins need to be properly folded and trafficked to their intended subcellular localization through subcellular targeting and sorting mechanisms, whose capacity has to be coordinated to match the rate of protein synthesis (Chartron et al., 2016; Jan et al., 2014; Lakkaraju et al., 2008). A primary subcellular trafficking mechanism of new proteins is the ER vesicular transport and secretory pathway through the endomembrane system, which is a rate-limiting step in the production of membrane and extracellular proteins. A mismatch between temporal synthesis rate and spatial localization capacity can lead to ER stress and subsequently mislocalization of newly synthesized proteins (Hetz et al., 2020).

Disruption of protein turnover and homeostasis is broadly implicated in human diseases including cardiomyopathies, cancer, and neurodegeneration (Hetz et al., 2020; Ren et al., 2021). In stressed cells, the accumulation of misfolded proteins triggers the unfolded protein response (UPR), which involves signaling pathways that suppress protein synthesis and promote protein folding and proteolysis to relieve proteostatic stress. At the same time, UPR activation invokes a spatial reorganization of the proteome, including but not limited to the transient translocation of UPR pathway mediators to the nucleus during initial stress response, the retrotranslocation of misfolded ER proteins to the cytosol for proteasomal clearance under endoplasmic-reticulum-associated protein degradation (ERAD), and the sequestration of RNA and RNA-binding proteins into stress granules. Despite ongoing

research, how the cellular proteome reorganizes under proteostatic stress remains incompletely understood, and the full scope of differentially localized proteins and pathways remains to be elucidated.

We wonder how the spatial and temporal regulations of proteins change in conjunction under UPR, such as whether proteins with differential spatial distributions are also differentially turned over. Advances in mass spectrometry methods have allowed the turnover rate and subcellular localization of proteins to be measured on a large scale. The turnover rate and half-life of proteins can be measured using stable isotope labeling in cells and in intact animals followed by mass spectrometry measurements of isotope signatures and kinetics modeling to derive rate constants (Claydon and Beynon, 2012; Doherty et al., 2009; Hammond et al., 2022; Schwanhäusser et al., 2011). Quantitative comparison of turnover rates provides a temporal view into proteostatic regulations and can implicate new pathological signatures and pathways over steady-state mRNA and protein levels (Andrews et al., 2022; Lam et al., 2014; Lau et al., 2018). In parallel, spatial proteomics methods have allowed increasing power to discern the subcellular localization of proteins on a large scale (Christopher et al., 2021; Geladaki et al., 2019; Kennedy et al., 2020; Mulvey et al., 2021; Orre et al., 2019). In recent work using a differential solubility fractionation strategy and mass spectrometry, we observed broad substantial rearrangement of proteins across three subcellular fractions in an acute paraquat challenge model of UPR in the mouse heart, consistent with protein translocation being an important layer of proteome regulation under proteostatic stress (Dostal et al., 2020). Nevertheless, an integrated strategy that can simultaneously measure protein turnover kinetics and spatial information has thus far not been realized.

Here we extended protein turnover measurements to include subcellular localization dynamics, by integrating dynamic SILAC labeling with differential ultracentrifugation-based spatial proteomics profiling strategies. We describe an experimental strategy and computational analysis pipeline to perform simultaneous proteome localization and turnover (SPLAT) measurements in baseline and stressed cells. SPLAT builds on prior work in protein turnover measurements and subcellular localization profiling, by combining dynamic SILAC isotope labeling, differential ultracentrifugation, isobaric TMT labeling, and kinetic modeling. This strategy allows for concurrent measurement of changes in the turnover dynamics and subcellular distributions of whole cell proteomes under perturbation in a single experiment. Applying this method to human AC16 cardiac cells under thapsigargin- and tunicamycin-induced UPR and to human induced pluripotent stem cell derived-cardiomyocytes (iPSC-CM) under carfilzomib induced proteasome inhibition, we delineated prominent changes in the spatial and temporal distributions of proteins on a proteome scale. The inclusion of spatial information of light and heavy SILAC labeled proteins moreover allowed disaggregation of the localization and trafficking of new and old protein pools.

117 # Results

118 **Simultaneous acquisition of turnover and spatial information using a double**
119 **labeling strategy**

120 We reason that we can use a hyperplexing strategy to simultaneously encode temporal and
121 spatial protein information through isotope labels in the MS1 and MS2 levels, respectively.
122 Hence, we designed a workflow that combines dynamic SILAC metabolic labeling in
123 cultured cells, with TMT labeling of spatially separated fractions to simultaneously measure
124 new protein synthesis as well as subcellular localization under baseline and perturbation
125 conditions (**Figure 1A**). To determine the rate of protein turnover during control,
126 thapsigargin, and tunicamycin conditions, a dynamic SILAC strategy was used to measure
127 the rate of appearance of post-labeling synthesized protein. Briefly, cells were pulsed with a
128 lysine and arginine depleted media supplemented with heavy labeled lysine and arginine
129 concurrently with drug treatment to label post-treatment synthesized proteins and derive
130 fractional synthesis rates through kinetic modeling.

131 Upon harvesting, the cells were fractionated to resolve subcellular compartments. We
132 adopted a protein correlation profiling approach. In particular, the LOPIT-DC (Localisation of
133 Organelle Proteins by Isotope Tagging after Differential ultraCentrifugation) method
134 (Geladaki et al., 2019) uses sequential ultracentrifugation to enrich different subcellular
135 fractions from the same samples, which facilitates ease of adoption and reproducibility.
136 Briefly, the cells were lysed under gentle conditions and then sequentially pelleted through
137 ultracentrifugation steps, which pellets subcellular fractions based on their sedimentation
138 rate and which is a function of particle mass, shape, and volume. The ultracentrifugation
139 fractions were each subsequently solubilized, and the extracted proteins were digested and
140 further labeled with tandem mass tag (TMT) isobaric stable isotope labels. The acquired
141 mass spectrometry data therefore carries temporal information in the dynamic SILAC tags
142 and spatial information in the TMT channel intensities (**Figure 1B**).

143 To process the double isotope encoded mass spectrometry data, we assembled a
144 custom computational pipeline comprising database search and post-processing, and
145 quantification for dynamic SILAC and TMT data (**Figure 1C**). The turnover kinetics
146 information from the dynamic SILAC data is analyzed using a mass spectrometry software
147 tool we previously developed, RIANA (Hammond et al., 2022), which integrates the areas-
148 under-curve of mass isotopomers from peptides over a specified retention time window, then
149 performs kinetic curve-fitting to a mono-exponential model to measure the fractional
150 synthesis rates (FSR) of each dynamic SILAC-labeled (K and R containing) peptide. To
151 extract the ultracentrifugation fraction quantification information for spatial analysis, we
152 developed a new version of the pyTMT tool which we previously described (Dostal et al.,
153 2020), and used it to perform TMT label quantification for the Comet/Percolator workflow. To
154 account for specific challenges related to spatial proteomics data features, we made two
155 new modifications. First, we account for isotope impurities in TMT tags. Because the TMT
156 data are row normalized in the LOPIT-DC design, we incorporated correction of isotope
157 contamination of TMT channels based on the batch contamination data sheet (**Supplemental**
158 **Table S1**) to account for isotope impurity in fractional abundance calculation from

159 randomized channels across experiments (**Supplemental Methods**). Second, we
160 implemented an isoform-aware quantitative rollup of peptide channel intensities into the
161 protein level for the downstream spatial proteomics analysis. Standard protein inference
162 invokes parsimony rules that assign peptides to the protein within a protein group with the
163 highest level of evidence, but razor peptides can conflate spatial information from different
164 proteins with different localization. Here the TMT-quantified peptides are summed into
165 protein groups using a more conservative aggregate method, such that the identified
166 peptides that are assigned to two or more top-level UniProt protein accessions are discarded
167 to avoid confounding of spatial information in the TMT channels. Moreover, protein groups
168 containing two or more proteins belonging to the same top-level UniProt accession are
169 removed from consideration if one of the non-canonical isoforms contain a unique peptide,
170 and are otherwise rolled up to the canonical protein. Protein isoforms are only included in
171 downstream analysis through quantified isoform-unique peptides. Following RIANA and
172 pyTMT processing, the SPLAT pipeline combines the dynamic SILAC and TMT information
173 by peptides and appends a heavy ("_H") tag to the UniProt accession of all peptides
174 containing dynamic SILAC modifications for separate localization analyses. The data were
175 then used for temporal kinetics summaries using the MS1 encoded information and
176 subcellular localization classification from the MS2 encoded information (**Figure 1D**). By
177 separately analyzing heavy and light peptides, the subcellular spatial information of the
178 heavy (new) and light (old) subpools of thousands of proteins can be mapped simultaneously
179 in normal and perturbed cells.

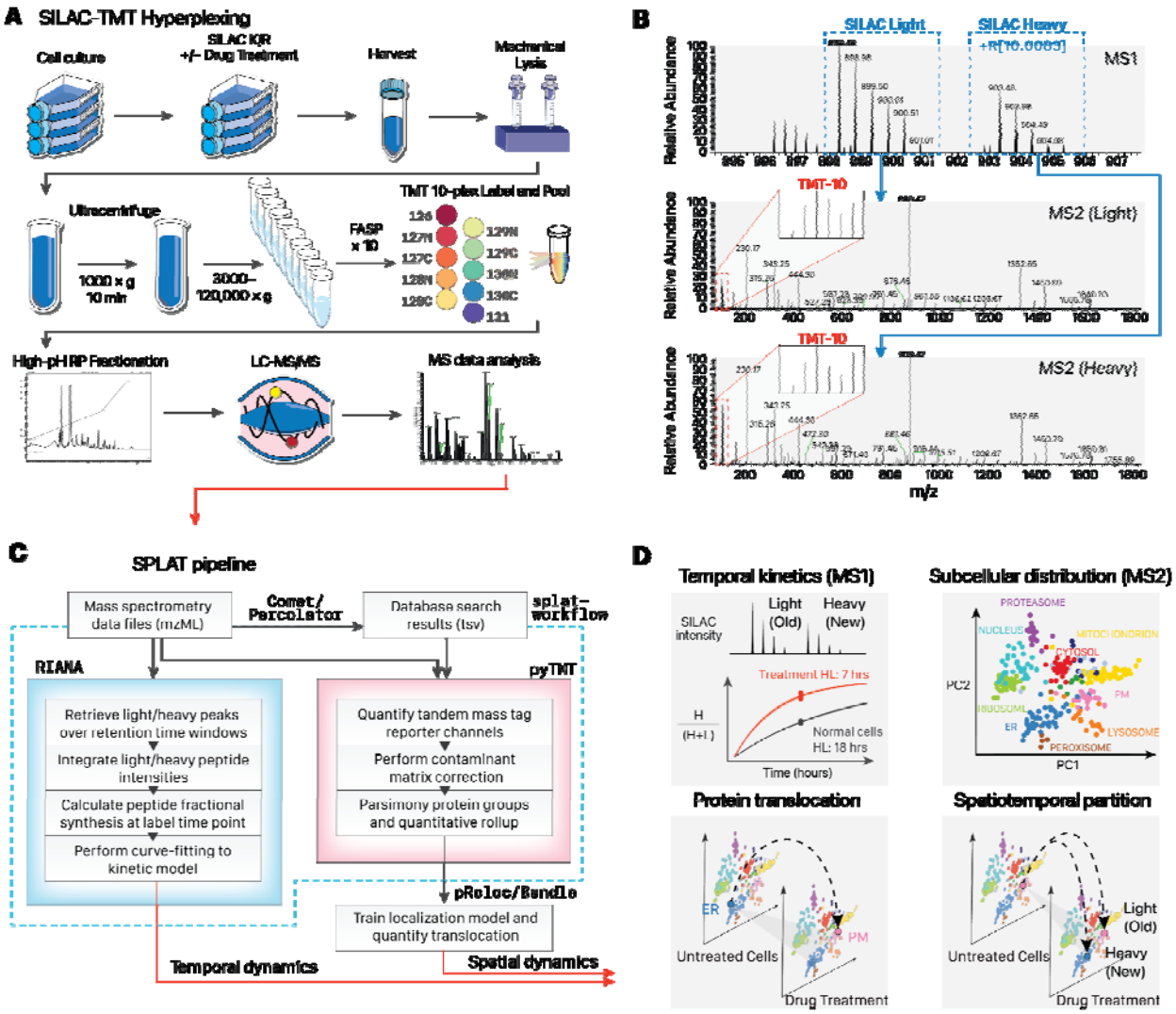

Figure 1. Overview of the SPLAT strategy. **A.** Experimental workflow. Control, thapsigargin-treated, and tunicamycin-treated human A16 cardiomyocytes were labeled with $^{13}C_6{}^{15}N_2$ L-Lysine and $^{13}C_6{}^{15}N_4$ L-Arginine dynamic SILAC labels. For each condition, 3 biological replicate SPLAT experiments were performed (n=3). After 16 hours, cells were harvested and mechanically disrupted, followed by differential ultracentrifugation steps to pellet proteins across cellular compartments. Proteins from the ultracentrifugation fractions were digested and labeled using tandem mass tag (TMT) followed by mass spectrometry. **B.** Dynamic SILAC labeling allowed differentiation of pre-existing (unlabeled, i.e., SILAC light) and post-labeling (heavy lysine or arginine, i.e., +R[10.0083]) synthesized peptides at 16 hours. The light and heavy peptides were isolated for fragmentation separately to allow the protein sedimentation profiles containing spatial information to be discerned from TMT channel intensities. **C.** Computational workflow. Mass spectrometry raw data were converted to mzML format to identify peptides using a database search engine. The mass spectra and identification output were processed using RIANA (left) to quantitate the time dependent change in SILAC labeling intensities and determine the protein half-life, and using pyTMT (right) to extract and correct TMT channel intensities from each light or heavy peptide MS2 spectrum. The TMT data were further processed using pRoloc/Bandle to predict protein subcellular localization via supervised learning. **D.** Temporal information and spatial information is resolved in MS1 and MS2 levels, respectively. SPLAT allows the

198 subcellular spatial information of the heavy (new) and light (old) subpools of thousands of proteins to
199 be quantified simultaneously in normal and perturbed cells. HL: Half-life.

200 Protein turnover kinetics regulations under unfolded protein response vary by 201 cellular compartments

202 We applied SPLAT to identify protein spatiotemporal changes in human AC16 cells under
203 UPR induced by 1 μM thapsigargin for 16 hours. Thapsigargin at the dosage and duration
204 used is a common and robust model to induce ER stress and integrated stress response in
205 cardiac and other cell types through the inhibition of sarco/endoplasmic reticulum Ca2+-
206 ATPase (SERCA). Thapsigargin treatment at 16 hours robustly induced known ER stress
207 markers (Glembotski, 2007) including BiP/HSPA5, HSP90B1, PDIA4 (limma FDR adjusted P <
208 0.01) (**Figure 2A**). Three biological replicate SPLAT experiments were carried out for normal
209 and thapsigargin-treated AC16 cells (n=3 each). We analyzed the spatial fractionation
210 patterns of the proteins following ultracentrifugation and TMT labeling, and classified the
211 subcellular localization of proteins using a Bayesian model BANDLE as previously described
212 (Crook et al., 2018). A spatial classification model is trained separately for each treatment
213 using a basket of canonical organelle markers (**see Methods**) which showed clear separation
214 in PC1 and PC2 in each condition (**Supplemental Figure S1**). The ultracentrifugation profiles
215 of each cellular compartment are highly consistent across treatments and replicates
216 (**Supplemental Figure S2**). To minimize the potential ratio compression that can result from
217 MS2-based TMT quantification, we employed extensive two-dimensional fractionation and
218 narrow isolation window, and verified that identified MS2 spectra had high precursor ion
219 purity (median purity 92–93%) (**Supplemental Figure S3**). We further performed a direct
220 comparison of MS2 and MS3 based quantification on an identical sample (control replicate 2)
221 (**Supplemental Figure S4**), which confirmed that MS2-based quantification produced
222 acceptable spatial resolution, consistent with previous observations (Shin et al., 2020).
223 In total using MS2-based TMT quantification, we mapped the subcellular profiles of
224 4360 protein features (i.e., 1,820 new and 2,540 old proteins) in normal AC16 cells across 3
225 biological replicate experiments using a stringent two-peptide filter at 1% FDR of protein
226 identification, with 1946 old proteins and 1,462 new proteins assigned to one of 12
227 subcellular localization with >95% confidence after removing outliers (see Methods) (**Figure**
228 **2B; Supplemental Data S1**). The accuracy of the spatial classification is supported by the
229 observation that 69.5% of assigned proteins in normal AC16 cells contain matching cellular
230 component annotation in Gene Ontology despite the current incompleteness of annotations
231 (**Figure 2C**) and 71.6% of proteins match their localization annotation in thapsigargin-treated
232 cells (**Supplemental Figure S5**). From the associated SILAC data of the proteins with spatial
233 information, we further quantified and compared the turnover kinetics of 2516 proteins
234 (**Supplemental Data S2**); hence we were able to acquire proteome-wide spatial and temporal
235 information in matching samples from a single experiment.
236 Considering the temporal kinetics data, we observed a proteome-wide decrease in
237 fractional synthesis rates under thapsigargin challenge compared with normal cells (median
238 protein half-life 46.9 vs. 19.9 hours; Mann-Whitney test P < 2.2e–16) (**Figure 2D**). This
239 slowdown is consistent with the extensive shutdown in protein translation due to ribosome

240 remodeling under integrated stress response (Bresson et al., 2020; Pakos-Zebrucka et al.,
241 2016), shown here by the decreased rate of SILAC incorporation into proteins.
242 Notwithstanding the overall slowdown, we also observed a wide range of protein turnover
243 rates in both the untreated and thapsigargin treated conditions that differ by the assigned
244 subcellular compartment (**Supplemental Figure S6**). Changes in protein kinetics following
245 thapsigargin also varies by compartment, with ER and Golgi proteins having significantly
246 less slowdown of protein kinetics compared to protein in other compartments (Mann-
247 Whitney test P: 9.4e–11 and 9.8e–5, respectively; << 0.05/13) (**Figure 2E**). On an individual
248 protein level, out of the 2516 proteins measured, 1542 showed significant changes in
249 temporal kinetics (Mann-Whitney test, FDR adjusted P value < 0.1), but the vast majority of
250 these proteins show decreases in turnover as expected, with only 12 proteins showing
251 significant increased temporal kinetics. Among these are the induced ER stress markers
252 BiP/HSPA5, HSP90B1, and PDIA4 (**Figure 2F; Supplemental Data S3**) but also other ER and
253 Golgi proteins that may be involved in stress response (**Figure 2G**). SDF2L1 (stromal-cell
254 derived factor 2 like 1) is recently described to form a complex with the ER chaperone
255 DNAJB11 to retain it in the ER (Hanafusa et al., 2019). In control cells, we found that SDF2L1
256 has a basal turnover rate of 0.027/hr. Upon thapsigargin treatment, its turnover rate
257 increased to 0.048 /hr (adjusted P: 0.07). DNAJB11 also experienced accelerated kinetics
258 (1.28-fold in thapsigargin, adjusted P 0.029) hence both proteins may be preferentially
259 synthesized during UPR. On a proteome level, gene set enrichment analysis (GSEA) of
260 temporal kinetics changes show a preferential enrichment of proteins in unfolded protein
261 response (FDR adjusted P: 4.1e–4), ER to Golgi anterograde transport (FDR adjusted P 0.036)
262 and N-linked glycosylation (FDR adjusted P: 1.7e–3) but a negative enrichment of translation-
263 related terms (**Figure 2H**). Overall, protein kinetic changes are modestly correlated with
264 protein abundance changes (**Supplemental Figure S7**), suggesting that AC16 cells actively
265 regulate protein synthesis and degradation kinetics in normal and stressed conditions
266 beyond changes in protein abundance.

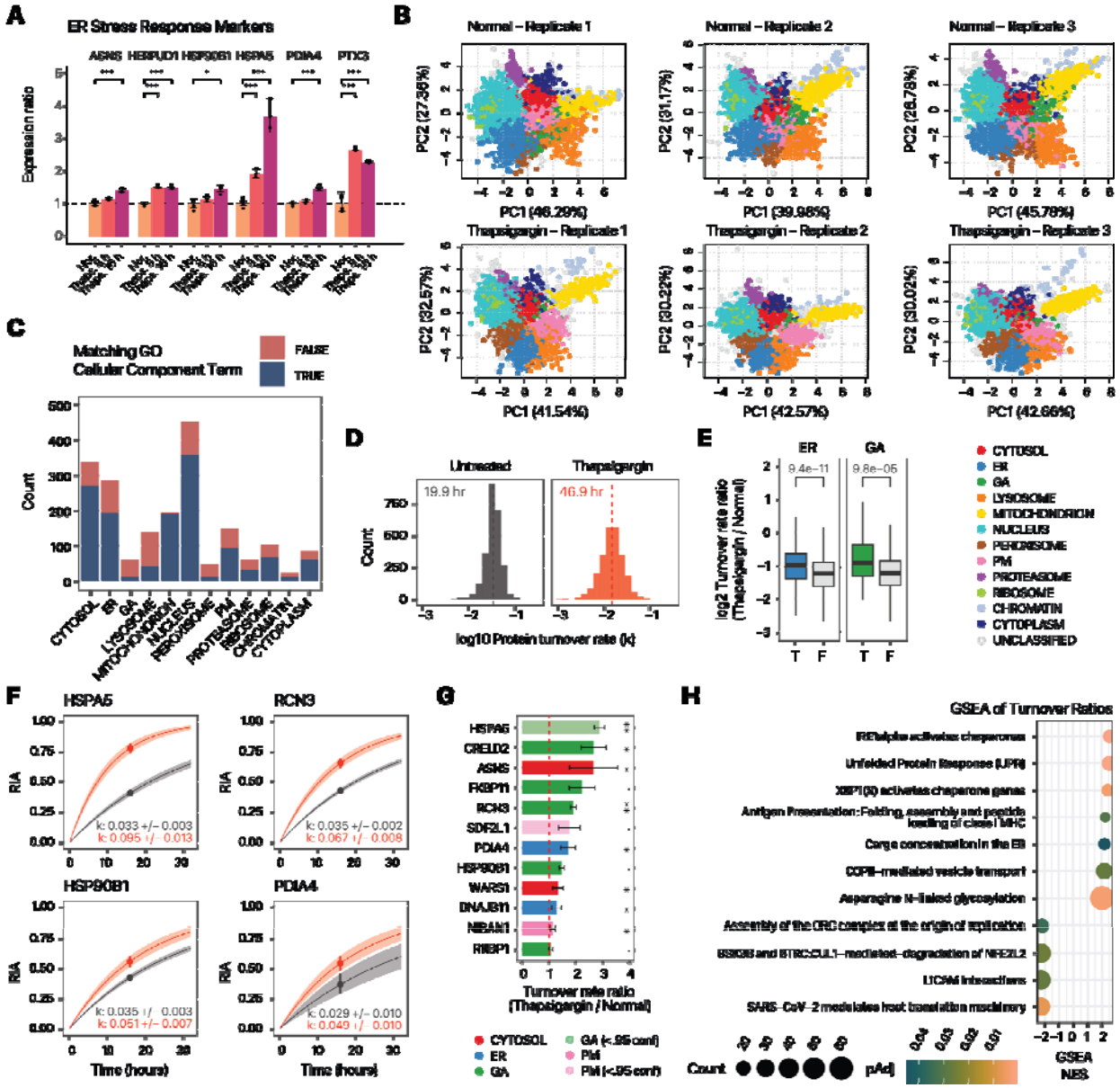

Figure 2. Simultaneous measurements of spatial and temporal kinetics under UPR. **A.** Bar charts showing activation of known ER stress markers upon thapsigargin treatment for 8 hours and 16 hours. X-axis: ER stress markers; y-axis: expression ratio (n=6 normal AC16; n=3 thapsigargin). *: limma adjusted P < 0.01; **: limma adjusted P < 0.001; ***: limma adjusted < 0.0001; error bars: s.d. **B.** PC1 and PC2 of proteins spatial map showing the localization of confidently allocated proteins in normal and thapsigargin-treated AC16 cells. Each data point represents a protein; color represents classification of subcellular localization. **C.** Distribution of light (unlabeled) protein features in each of the 12 subcellular compartments (n=3); fill color represents whether the protein is also annotated to the same subcellular compartment in UniProt Gene Ontology Cellular Component terms. **D.** Histograms of the determined log10 protein turnover rates in control and thapsigargin treated cells (n=3). Text overlay indicates median half-life. **E.** Boxplot showing the log2 turnover rate ratios in thapsigargin over normal AC16 cells for proteins that are localized to the ER (blue) (T) or not (F); or the Golgi (GA; green). P values: Mann-Whitney test. A Bonferroni corrected threshold of 0.05/13 is considered significant. Center line: median; box limits: interquartile range; whiskers: 1.5x interquartile

range. **F.** Example of best fit curves in the first-order kinetic model at the protein level between normal (gray), and thapsigargin treated (red) AC16 cells showing four known ER stress markers with elevated turnover (HSPA5, RCN3, HSP90B1, and PDIA4). Because the sampling time point is known, the measured relative isotope abundance of a peptide (prior to reaching the asymptote) is sufficient to define the kinetic curve and the parameter of interest (k). **G.** Turnover rate ratio (thapsigargin vs. normal) of the top proteins with elevated temporal kinetics in UPR within the ER (blue) and Golgi (green); .: Mann-Whitney test FDR adjusted P value < 0.1; *: < 0.05; ** < 0.01; red dashed line: 1:1 ratio; bars: standard error. **H.** Gene set enrichment analysis (GSEA) of turnover rate ratios in thapsigargin treatment; proteins with faster kinetics are significantly enriched in DNA damage response and UPR pathways. Color: FDR adjusted P values in GSEA; x-axis: GSEA normalized enrichment score (NES). Size: number of proteins in gene set.

Changes in protein subcellular distribution under ER stress

We next analyzed the spatial proteomics component of the data to find proteins that change in their subcellular localization following thapsigargin treatment. To do so, we used a Bayesian statistical model implemented in the BANDLE package to estimate the differential spatial localization of proteins. In total, we identified 1,306 translocating protein features (687 light and 619 heavy) in thapsigargin under a stringent filter of BANDLE differential localization probability > 0.95 with an estimated FDR of 0.0018 (0.18%), and further filtered using a bootstrap differential localization probability of > 0.95. We then further prioritized 330 pairs of differentially localized proteins where the light and heavy features both show confident differential localization (**Supplemental Data S2**, **Supplemental Data S4**). The differential localization of these 330 proteins recapitulate previously established relocalization events in cellular stress response, capturing the migration of caveolae toward the mitochondrion under cellular stress (Fridolfsson et al., 2012) (**Supplemental Figure S8A)**, and the engagement of EIF3 to ribosomes in EIF3-dependent translation initiation in integrated stress response (Guan et al., 2017) (**Supplemental Figure S8B**), thus supporting the confidence of the spatial translocation assignment.

From the results, we discerned three major categories of differential localization behaviors in ER stress that revealed new insights into proteome-wide features of UPR. First, we observed the externalization of proteins toward the plasma membrane (**Figure 3A**). The large neutral amino acid transporter component SLC3A2 is localized to the lysosome fraction in normal cells (Pr > 0.999) but in thapsigargin-treated cells is localized confidently to the plasma membrane (BANDLE differential localization probability > 0.999) (**Figure 3B**). Showing similar behaviors are SLC7A5, the complex interacting partner of SLC3A2; and two other amino acid transporters SLC1A4, and SLC1A5 (**Figure 3C**); whereas the ion channel proteins SLC30A1, ATP1B1, ATB1B3 and ATP2B1 also showed confident localization toward the cell surface (**Figure 3C**). The change in localization of SLC3A2 is corroborated by immunostaining (**Figure 3D**), which shows a decrease in co-localization between immunostaining signals of SLC3A2 and lysosome marker LAMP2 upon thapsigargin treatment (**Figure 3E**).

Second, thapsigargin treated AC16 cells are associated with an increase in proteins classified into the peroxisome fraction including proteins whose locations changed from the ER, Golgi, and the nucleus in normal cells (**Figure 3F**). In mammalian cells, ER and

325 peroxisomes are spatially adjacent; the peroxisome associated fractions sediment
326 prominently at 5000–9000 × g (F3 and F4) in the LOPIT-DC protocol (**Supplemental Figure**
327 **S2**), marked by canonical peroxisome markers PEX14 and ACOX1 (**Supplemental Data S2**).
328 However, although this compartment was trained using peroxisome markers, the majority of
329 proteins categorized into this compartment are not annotated to be in the peroxisome
330 whereas 30 out of 49 (61%) of proteins in the control cells allocated to this compartment were
331 annotated also as endosome, including canonical markers EEA1 and VPS35L. We thus refer
332 to this compartment hereafter as peroxisome/endosome. Moreover, proteins that become
333 differentially localized to this fraction in thapsigargin include known stress granule proteins
334 UBAP2, USP10, CNOT1, CNOT2, CNOT3, CNOT7, CNOT10, ZC3H7A, and NUFIP2 (**Figure 3G**
335 **and Supplemental Figure S9)**, which show high-confidence translocation to the
336 peroxisome/endosome fraction, and are known RNA binding proteins that participate in
337 phase separation, consistent with stress granule formation in UPR. Notably, LMAN1,
338 LMAN2, SCYL2, and SNX1 are RNA-binding proteins that are not currently established stress
339 granule components and show identical translocation patterns, nominating them as
340 potential participants in RNA granule related processes in AC16 cells for further studies
341 (**Supplemental Figure S9**). Other proteins in this fraction include the ER-to-Golgi transport
342 vesicle proteins GOLT1B, GOSR2, RER1, and NAPA (**Supplemental Figure S9**).
343 Lastly, we see evidence of proteins from the ER and Golgi targeted to the lysosome
344 (see Tunicamycin section below). Thus taken together, the spatial proteomics component of
345 the data reveals a complex network of changes in protein spatial distribution during UPR.

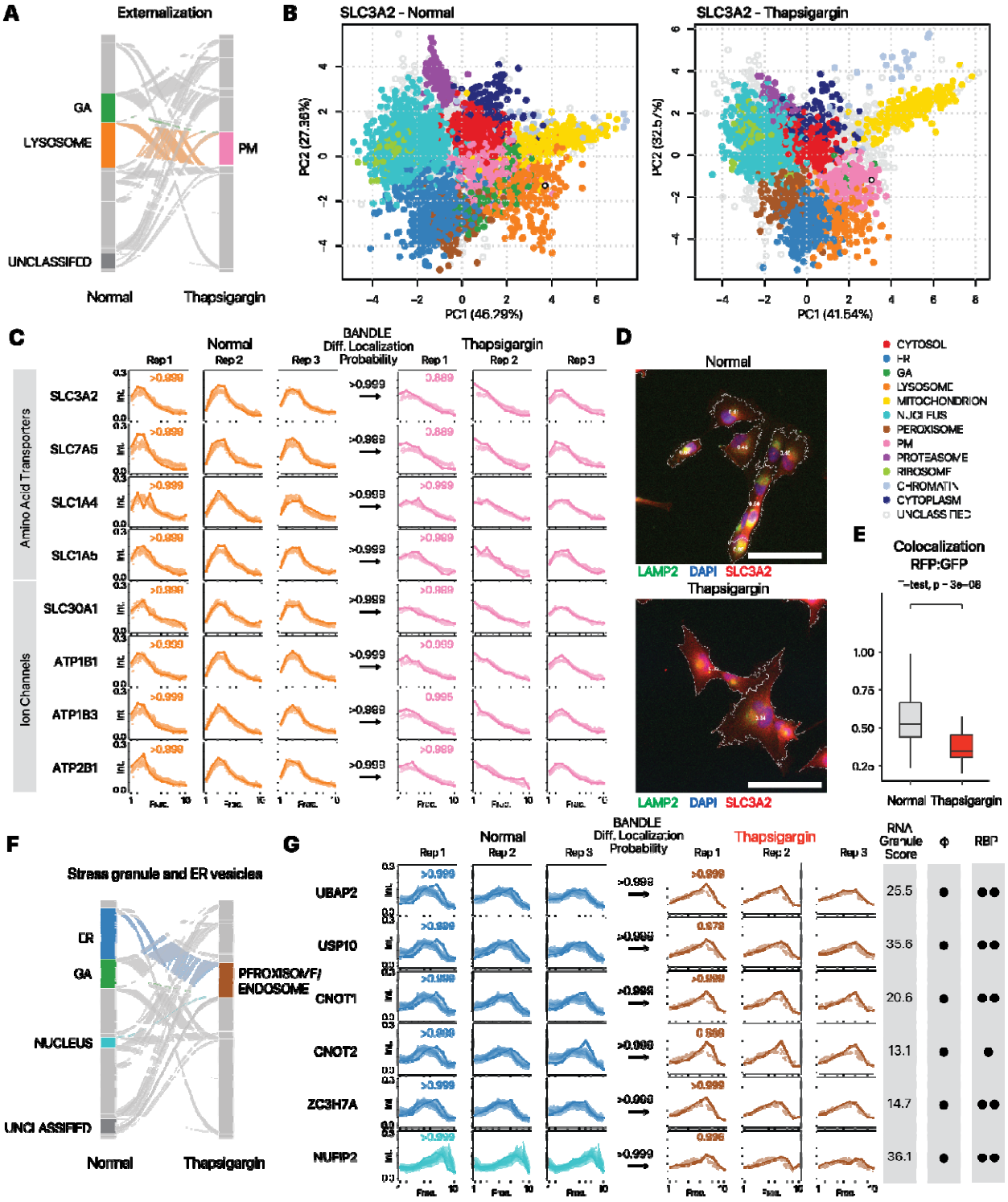

Figure 3. SPLAT captures extensive protein translocation in AC16 cells under UPR. **A.** Alluvial plot of translocation events (> 0.99 BANDLE translocation probability; estimated FDR < 1%) following thapsigargin treatment showing a cohort of proteins moving from the Golgi apparatus (GA) and lysosome towards the plasma membrane (PM) (n=3). **B.** Protein spatial map for SLC3A2 (open black circle) in normal (left) and thapsigargin-treated (right) AC16 cells, showing its colocalization with lysosomal proteins in normal cells and in PM proteins in thapsigargin-treated cells. Colors represent

allocated subcellular localization. **C.** Ultracentrifugation fraction profile of SLC3A2 and other amino acid transporters SLC7A5, SLC1A4, SLC1A5 and ion channel proteins SLC30A1, ATP1B1, ATP1B3, and ATP2B1 with similar migration patterns. X-axis: fraction 1 to 10 of ultracentrifugation. Y-axis: relative channel abundance. Bold lines represent the protein in question; light lines represent ultracentrifugation profiles of all proteins classified to a respective localization. Colors correspond to subcellular localization in panel B and for all AC16 data throughout the manuscript; numbers within boxes correspond to BANDLE allocation probability to compartment. **D.** Immunofluorescence of SLC3A2 (red) against the lysosome marker LAMP2 (green) and DAPI (blue). Numbers in cell boundary: colocalization score per cell. Scale bar: 90 μm. **E.** Colocalization score (Mander's correlation coefficient) between SLC3A2 and LAMP2 decreases significantly (two-tailed unpaired t-test P value: 3e–8) following thapsigargin treatment, consistent with movement away from lysosomal fraction (n= 205 normal cells, n = 32 thapsigargin treated cells). Center line: median; box limits: interquartile range; whiskers: 1.5x interquartile range; points: outliers. **F.** Alluvial plot showing the migration of ER, GA, and nucleus proteins toward the peroxisome/endosome containing fraction in thapsigargin treated cells. **G.** Ultracentrifugation fraction profile of stress granule proteins UBAP2, USP10, CNOT1, CNOT2, ZC3H7A, and NUFIP2. RNA Granule Score: score from RNA Granule Database (https://rnagranuledb.lunenfeld.ca/). A score of 7 or above is considered a known stress granule protein. Phi: predicted phase separation participation. Circle denotes a prediction of True within the database. RBP: Annotated RNA binding protein on the RNA Granule Database. One circle denotes known RBP in at least one data set; two circles denote known RBP in multiple datasets.

Partition of newly synthesized and pre-existing protein pools

We next considered the interconnectivity of temporal and spatial dynamics, namely whether some localization changes are contingent upon protein pool lifetime, such as where light (old) protein does not change in spatial distribution but the heavy (new) proteins display differential translocation upon UPR. Because the spatial profiles of the light and heavy proteins are acquired independently, this experimental design allowed us to examine whether old and new proteins are localized to identical cellular locales. In both normal and thapsigargin-treated cells, we found that the independently measured spatial profiles of light (pre-existing) proteins and their corresponding heavy SILAC (newly synthesized) counterparts are highly concordant, with a normalized spatial distribution distance (see Supplemental Methods) of 0.020 [0.015 – 0.030], compared to 0.117 [0.080 – 0.155] in random pairs of pre-existing proteins (1,614 light-heavy pairs, Mann-Whitney $P < 2.2e–16$) in normal cells, and 0.028 [0.019 – 0.041] and 0.122 [0.081 – 0.161] in thapsigargin-treated cells (1,614 light-heavy pairs, Mann-Whitney $P < 2.2e–16$) (**Figure 4A**). This robust agreement provided an additional independent confirmation on the accuracy of the spatial measurements. Consistently, among heavy-light protein pairs with confidently assigned subcellular localization, the heavy and light proteins are assigned to the identical subcellular compartment in 93% and 89% of the cases in normal and thapsigargin-treated AC16 cells, respectively (**Figure 4B**). We focused on the unusual cases where the spatial distribution distances between the heavy and light proteins increased noticeably following thapsigargin treatment, as they may be indicative of localization changes that are dependent upon time since synthesis. These include two proteins EGFR and ITGAV with an uncommon increase in heavy-light spatial distances (Z: 12.00 and 2.24, respectively) (**Figure 4C**). Epidermal growth factor receptor (EGFR/ErbB1/HER1) is a receptor tyrosine kinase with multiple subcellular

397 localizations and signaling roles, and is implicated in cardiomyocyte survival (Lee et al.,
398 2020). Following a variety of stressors, EGFR is known to be inactivated by intracellular
399 trafficking, including being internalized to the early endosome and lysosome following
400 oxidative stress and hypoxia in cancer cells (Tan et al., 2016). In the spatial proteomics data,
401 the spatial distribution of EGFR borders the lysosome and plasma membrane fractions,
402 which we interpret as EGFR having potential multiple pools including a cell surface fraction
403 (**Figure 4D**). In the thapsigargin treated cells, the light-heavy spatial distance of EGFR
404 increased from 0.014 in normal cells to 0.052, and the dynamic SILAC labeled pool (heavy)
405 becomes internalized toward the ER (BANDLE differential localization probability: >0.999)
406 but not the pre-existing (light) pool (**Figure 4E**). The data therefore suggests that the
407 internalization of EGFR under thapsigargin is likely to be due to endomembrane stalling or
408 redistribution upon new protein synthesis, possibly leading to fewer new EGFR molecules
409 reaching the cell surface. Likewise, in thapsigargin-treated AC16 cells, newly-synthesized
410 ITGAV (integrin subunit alpha V) shows a partition from the plasma membrane fraction to
411 the ER fraction but not the old/existing protein pool, concomitant with an increase in spatial
412 distribution distance from 0.017 to 0.057 between old and new proteins (**Figure 4F–G**). With
413 the function of integrins as cell surface receptors that function in intracellular-to-extracellular
414 and retrograde communication, the ER localization of newly synthesized ITGAV, such as due
415 to stress-induced stalling of protein trafficking along the secretory pathway, could indicate a
416 decrease in integrin signaling function through spatial regulation rather than protein
417 abundance. To partially corroborate the partial redistribution of EGFR, we performed
418 immunocytochemistry imaging of EGFR subcellular distribution in AC16 cells with or
419 without thapsigargin (**Figure 4H**). Thapsigargin treatment did not increase cell size (**Figure**
420 **4I**), and whereas there is an increase in immunofluorescence signal of EGFR in thapsigargin
421 (**Figure 4J**), this signal is distributed preferentially to the interior of the cell such that there is
422 a significant reduction in the ratio of mean intensity at cell borders over the whole cell in
423 thapsigargin vs. untreated cells (0.673 vs. 0.746, n=93 and 71 cells, Mann-Whitney P: 1.7e–4)
424 (**Figure 4K**), consistent with a partial redistribution of EGFR toward an internal pool. Taken
425 together, these examples demonstrate the SPLAT strategy can be used to distinguish time-
426 dependent differential localization of proteins such as due to the trafficking of newly
427 synthesized proteins.
428
429
430

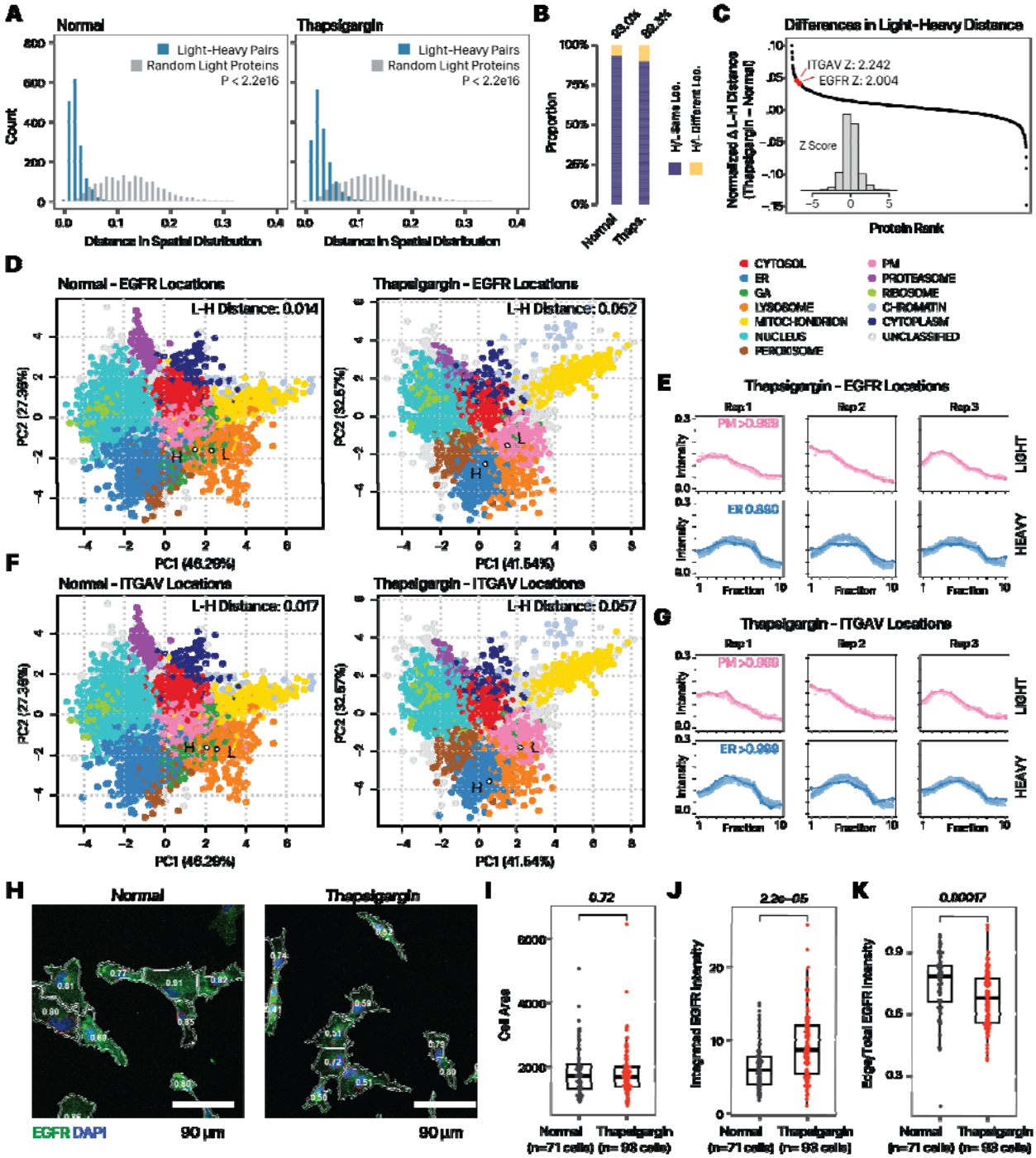

Figure 4. SPLAT reveals protein-lifetime dependent translocation. **A.** Histogram showing the similarity in light and heavy proteins in normalized fraction abundance profiles in (left) normal and (right) thapsigargin-treated AC16 cells. X-axis: the spatial distribution distance of two proteins is measured as the average euclidean distance of all TMT channel relative abundance in the ultracentrifugation fraction profiles across 3 replicates; y-axis: count. Blue: distance for 1,614 quantified light-heavy protein pairs (e.g., unlabeled EGFR, heavy SILAC-labeled EGFR). Grey: distribution of each corresponding light protein with another random light protein. P value: Mann-Whitney test. **B.** Proportion of heavy-light protein pairs with confidently assigned localization that are assigned to the same location (purple) in normal (left; 93%) and thapsigargin-treated (right; 89%) cells.

441 **C.** Ranked changes in heavy-light pair euclidean distance upon thapsigargin treatment. The difference
442 in heavy-light distances in thapsigargin is adjusted by the average changes in the spatial distance of
443 the light protein with 250 other sampled light proteins to calculate the normalized difference. The
444 majority of proteins show no change (+/- 0.02 in euclidean distance). The positions of EGFR and
445 ITGAV are highlighted. Inset: Z score distribution of all changes. **D.** Spatial map showing the location
446 of the light and heavy EGFR in normal and thapsigargin-treated AC16 cells. Each data point is a light
447 or heavy protein species. Colors correspond to other AC16 experiments in the manuscript. Numbers
448 correspond to euclidean distance in fraction profiles over 3 replicates. **E.** Corresponding fraction
449 profiles; x-axis: ultracentrifugation fraction; y-axis: fractional abundance. Post-labeling synthesized
450 EGFR is differentially distributed in thapsigargin and shows ER retention (blue), whereas the
451 preexisting EGFR pool remains to show a likely cell surface localization (pink) after thapsigargin. **F-G**.
452 As above, for ITGAV. **H.** Confocal imaging of EGFR immunofluorescence supports a partial
453 relocalization of EGFR from the cell surface toward internal membranes following thapsigargin
454 treatment. Numbers: The mean intensity of the labeled EGFR channel of a 3 pixel border at cell
455 boundaries was divided by mean intensity of the whole cell to estimate the ratio of EGFR at the
456 plasma membrane to the cell interior. Blue: DAPI; Green: EGFR; scale bar: 90 μm. **I.** Cell areas; Mann-
457 Whitney P: 0.72. Center line: median; box limits: interquartile range; whiskers: 1.5x interquartile range.
458 **J.** Total EGFR intensity per cell; Mann-Whitney P: 2.2e-05. Center line: median; box limits: interquartile
459 range; whiskers: 1.5x interquartile range. **K.** Edge/total intensity ratios in normal and thapsigargin-
460 treated AC16 cells (n=71 normal cells; n=93 thapsigargin cells; Mann-Whitney P: 1.7e–4). Center line:
461 median; box limits: interquartile range; whiskers: 1.5x interquartile range.

462 Spatiotemporal proteomics highlights similarities and differences of ER stress 463 induction protocols

464 We next investigated the protein spatiotemporal features of AC16 cells under the treatment
465 of tunicamycin, another compound commonly used to induce ER stress in cardiac cells (Liu et
466 al., 2012; Toro et al., 2022) by inducing proteostatic stress via inhibition of nascent protein
467 glycosylation. Three biological replicate SPLAT experiments were performed in tunicamycin-
468 treated cells to resolve the temporal kinetics and subcellular localisation of proteins
469 (**Supplemental Figures S1, S2C, S5B, S6, S7B, S10**). Tunicamycin treatment at 1 μg/mL for 16
470 hours robustly induced the known ER stress response markers BiP/HSPA5, HSP90B1, PDIA4,
471 CALR, CANX, and DNAJB11 (limma FDR adjusted P < 0.10) (**Figure 5A**) demonstrating
472 effective ER stress induction. Overall, tunicamycin treatment led to a lesser slowdown of
473 temporal kinetics than thapsigargin (average protein half-life 32.6 hours) (**Figure 5B;**
474 **Supplemental Data S5**). As in thapsigargin treatment, the kinetic changes following
475 tunicamycin are different across cellular compartments, with ER and Golgi proteins having
476 relatively faster kinetics than other cellular compartments (Mann-Whitney test P: 1.3e–13 and
477 6.6e–5; << Bonferroni corrected threshold 0.05/13); whereas the greatest reduction was
478 observed among proteins localized to the lysosome, a compartment closely linked to
479 glycosylation and recycling of glycans (Mann-Whitney test P: 1.8e–10) (**Figure 5C**). Gene set
480 enrichment analysis (GSEA) of turnover rate ratios revealed a significant positive enrichment
481 of UPR proteins (adjusted P 3.5e–3) and DNA repair terms (e.g., processing of DNA double-
482 strand break ends; adjusted P 0.017) and a negative enrichment of translation related terms
483 (**Figure 5D**). Compared to thapsigargin treatment however, no significant enrichment of
484 glycosylation and vesicle transport related terms were found in tunicamycin. Inspection of

485 individual protein kinetics changes likewise revealed both similar induction of the ER stress
486 response markers HSPA5, HSP90B1 and PDIA4 as in thapsigargin treatment, but other stress
487 response genes PDIA3 and NIBAN1 are not induced in thapsigargin (**Figure 5E**). On the
488 other hand, RCN3 (reticulocalbin 3) is an ER lumen calcium binding protein that regulates
489 collagen production (Martínez-Martínez et al., 2017) and shows increased temporal kinetics
490 in thapsigargin (**Figure 2F**) but not in tunicamycin (ratio 0.76 over normal; **Supplemental**
491 **Data S5**), altogether reflecting potential differences in stress response modality to a different
492 ER stress inducer.
493 Parallel to the less prominent changes in vesicle transport, tunicamycin treatment
494 also led to fewer translocating proteins than thapsigargin, with 620 translocating features
495 (including 282 light proteins and 338 heavy proteins) at BANDLE differential localization
496 probability > 0.95, corresponding to an estimated FDR of 0.35%, and thresholded by
497 bootstrapping differential localization probability > 0.95; from which we highlighted 109
498 proteins where the heavy and light versions both showed translocation. The spatial data
499 revealed a high degree of similarity but also notable differences with thapsigargin-induced
500 ER stress. We found that in both tunicamycin and thapsigargin treatment, there was
501 evidence of lysosome targeting from other endomembrane compartments, including: RRBP1,
502 a ribosome-binding protein of the ER, GANAB, a glucosidase II alpha subunit integral to the
503 proper folding of proteins in the ER, FKBP11, a peptidyl-prolyl cis/trans isomerase important
504 to the folding of proline-containing peptides, IKBIP, an interacting protein to the IKBKB
505 nuclear kinase, and MANF, a neurotrophic factor which has relations to ER stress-related cell
506 death when its expression is lowered (BANDLE differential localization probability > 0.999)
507 (Sayers et al., 2022) (**Figure 5F**). Among these proteins was the collagen synthesis enzyme
508 P3H1 in both thapsigargin and tunicamycin. Interestingly, prior work found no correlation
509 between the protein abundance of collagen modifying enzymes with the known reduction of
510 collagen synthesis in chondrocytes and fibroblasts under ER stress (Vonk et al., 2010). The
511 results here suggest that the functional decline may instead correlate with a change in the
512 subcellular localization of collagen modifying enzymes in AC16 cells. Tunicamycin treatment
513 also induced old-new protein partitions in EGFR and ITGAV as observed in thapsigargin
514 (**Supplemental Figure S11**). Notably, although tunicamycin also induced the translocation of
515 proteins toward the peroxisome/endosome fraction, different proteins are involved, including
516 the stress response proteins DNAJB11, DNAJC3, DNAJC10, and PDIA6 as well as other
517 proteins EMC4, EMC8, VAPA, and VAPB (**Supplemental Figure S12**) which further outlines
518 different modalities of cellular response toward two different ER stress inducers. The
519 translocating stress response proteins DNAJB11, DNAJC10, and PDIA6 also showed
520 significant acceleration in temporal kinetics in tunicamycin (Mann-Whitney test, FDR
521 adjusted $P < 0.10$; **Supplemental Data S6**) which is consistent with specific production of
522 the proteins followed by shuttling to subcellular location for their function during stress
523 response.

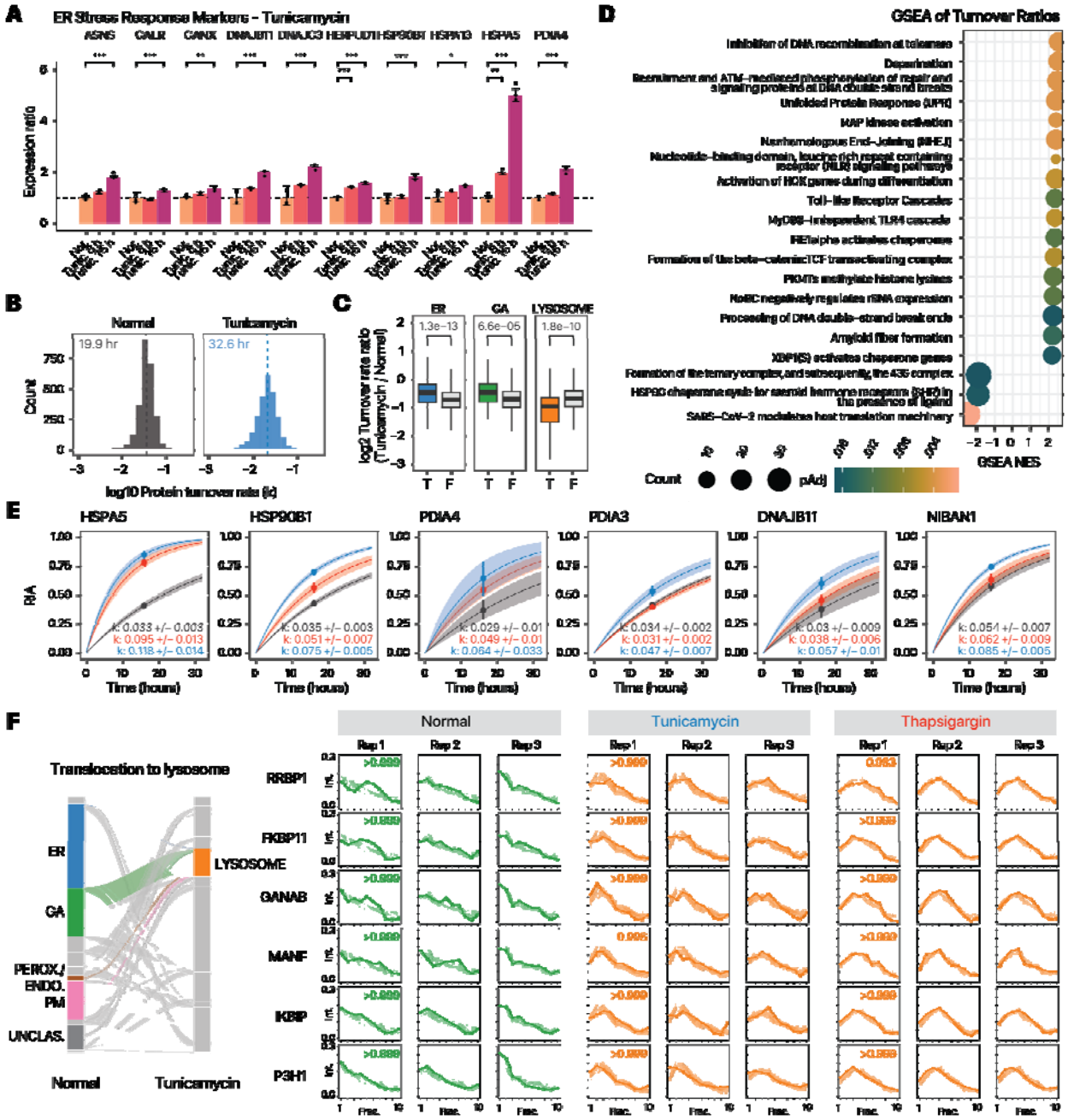

Figure 5. Comparison of ER stress induction methods. **A.** Bar charts showing activation of known ER stress markers upon tunicamycin treatment for 8 hours and 16 hours. X-axis: ER stress markers; y-axis: expression ratio (n=6 normal AC16; n=3 tunicamycin). *: limma adjusted P < 0.01; **: limma adjusted P < 0.001; ***: limma adjusted P < 0.0001; error bars: s.d.. **B.** Histograms of the determined log10 protein turnover rates in control and tunicamycin treated cells (n=3). **C.** Boxplot showing the log2 turnover rate ratios in tunicamycin over normal AC16 cells for proteins that are localized to the ER (T) or not (F); Golgi apparatus, or the lysosome. P values: two-tailed t-test. Center line: median; box limits: interquartile range; whiskers: 1.5x interquartile range. A Bonferroni corrected threshold of 0.05/13 is considered significant. **D.** Gene set enrichment analysis (GSEA) of turnover rate ratios in tunicamycin treatment. Color: FDR adjusted P values in GSEA; x-axis: GSEA normalized enrichment score (NES). Size: number of proteins in the gene set. **E.** Example of best fit curves in the first-order kinetic model at

the protein level between normal (gray), tunicamycin (blue) and thapsigargin (red) treated AC16 cells showing known ER stress markers with elevated turnover in both ER stress inducers (HSPA5, HSP90B1, and PDIA4) as well as stress response proteins with elevated turnover only in tunicamycin (PDIA3, DNAJB11, NIBAN1). **F.** Alluvial plot showing the migration of ER, GA, and peroxisome/endosome proteins toward the lysosome (left). On the right, the ultracentrifugation fraction profiles of translocating proteins RRBP1, FKBP11, GANAB, MANF, IKBIP, and P3H1 are shown that are targeted toward the lysosome in both tunicamycin and thapsigargin treatment (BANDLE differential localization probability > 0.95). Numbers in boxes are the BANDLE allocation probability in each condition (n=3).

Application of SPLAT to the mechanism of cardiotoxicity in iPSC-CM models

We next assessed the applicability of SPLAT toward a different, non-proliferating cell type (human iPSC-derived cardiomyocytes [iPSC-CMs]) and its utility for interrogating the mechanism of cardiotoxicity following proteasome inhibitor treatment (**Figure 6A**). The ubiquitin proteasome system is responsible for the degradation of over 70% of cellular proteins. Compounds that inhibit proteasome function, including carfilzomib, are widely used as cancer treatment and have led to remarkable improvement in the survival of multiple myeloma patients. Mechanistically, carfilzomib functions by binding to and irreversibly inhibiting the proteasome catalytic subunit PSMB5 (Cromm and Crews, 2017), leading to the accumulation of unfolded proteins in cancer cells. Importantly, despite its efficacy as a cancer treatment, carfilzomib also leads to cardiotoxic adverse effects including heart failure (<20%), arrhythmia (<10%), and hypertension (11-37%) in a significant number of patients (IBM Watson Health, 2023). This cardiotoxicity has been modeled in vitro by exposure of 0.01 – 10 μM carfilzomib to human iPSC-CMs (Forghani et al., 2021), yet the molecular mechanisms of carfilzomib cardiotoxicity remain incompletely understood. To examine the protein spatiotemporal changes upon carfilzomib-mediated proteasome inhibition in cardiac cells, we differentiated contractile iPSC-CMs using a small molecule based protocol, and treated the cells with 0.5 μM carfilzomib. To verify toxicity modeling, we measured iPSC-CM viability and phenotypes under 0 to 5 µM carfilzomib for 24 and 48 hours. Under the chosen treatment (0.5 µM for 48 hours), iPSC-CMs showed sarcomeric disarray consistent with prior observations on the cardiotoxic effects of carfilzomib (**Figure 6B**) but maintained viability (82%) (**Figure 6C**), while showing significant decreases in oxygen consumption (**Figure 6D**), basal respiration (**Figure 6E)**, and maximal respiration (**Figure 6F**), whereas higher doses are accompanied with drops in viability at 48 hours and an increase in proton leak (**Figure 6G**). ATP production at the 0.5 µg dose was significantly lower than untreated cells at both 24 and 48 hours (**Figure 6H**). Therefore cardiotoxicity due to carfilzomib can be recapitulated in a human iPSC-CM model, consistent with prior work in the literature.

From the untreated and carfilzomib-treated (0.5 μM, 48 hrs) human iPSC-CMs, we constructed a protein subcellular spatial map that takes into account several features of the iPSC-CM cell type, including the inclusion of cell junction and desmosome proteins, as well as a sarcomere protein compartment, that are not apparently recognized as discrete compartments in the prior spatial maps (**Supplemental Figure S13**). In addition, the 40S and 60S ribosomes showed clear separation in iPSC-CM unlike in AC16 cells and are hence classified separately. This separation is consistent with less active protein translation in this

cell type. In total, we mapped the subcellular localization of 5,047 protein features including 2,680 old proteins and 2,367 new proteins using a stringent two-peptide filter at 1% FDR of protein identification, including 2,010 old proteins and 1,737 new proteins assigned to one of 13 subcellular localization with >95% confidence after removing outliers (**Figure 6I; Supplemental Data S7**). The iPSC-CM spatial map achieved similar levels of concordance with known cellular component annotations as in AC16 cells (70.8% with known annotation matching the assigned compartment in normal iPSC-CM; 63.0% in carfilzomib-treated cells) (**Supplemental Figure S14**). The iPSC-CM map has comparable spatial distance between light and heavy protein pairs as in AC16 cells, and 87.6% heavy-light protein pairs map to the same compartment in the baseline, supporting that there is sufficient spatial resolution to resolve subcellular compartment differences in this cell type (**Supplemental Figure S14**).

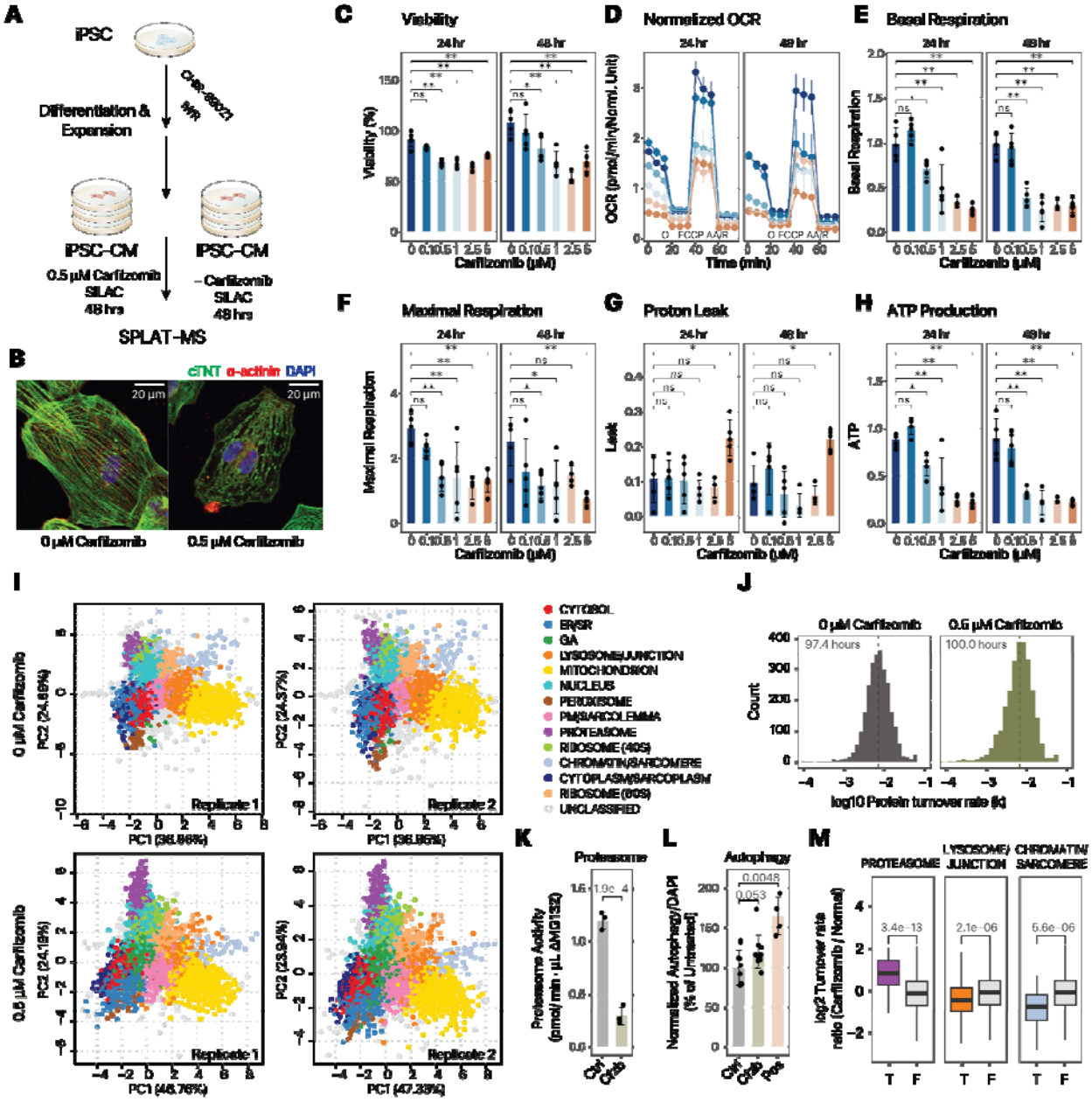

591 **Figure 6. Applicability in human iPSC-derived cardiomyocytes. A.** Schematic of human iPSC
592 differentiation into cardiomyocytes, carfilzomib treatment, and SPLAT analysis. **B.** Confocal
593 microscopy images showing sarcomeric disarray in iPSC-CMs upon 48 hrs of 0.5 μM carfilzomib;
594 green: cTNT, red: alpha-actinin; blue: DAPI; scale bar: 20 μm. **C–H.** Cell viability (%), normalized
595 Seahorse oxygen consumption rate (OCR; pmol/min), basal respiration, maximal respiration, proton
596 leak, and ATP production upon 0 – 5 μM carfilzomib for 24 or 48 hrs; .: adjusted $P < 0.1$; *: adjusted $P <$
597 0.05; **: adjusted $P < 0.01$, ANOVA with Tukey's HSD post-hoc at 95% confidence level; n=5. Error
598 bars: s.d. for bar charts in panels C, E, F, G, H; s.em. for the OCR graph in panel D. Colors in panel D:
599 dosage, same as panel C. O: Oligomycin; AA/R: Antimycin A/Rotenone. **I.** Spatial map with 13
600 assigned subcellular localizations in iPSC-CMs at the baseline (top) and upon 0.5 μM carfilzomib
601 treatment (n=2). **J.** Histogram of log10 protein turnover rates (k), with median half-life of 97.4 hours
602 and 100.0 hours in normal and carfilzomib-treated iPSC-CM. **K.** Proteasome activity in iPSC-CMs
603 treated with 0 (Ctrl) vs. 0.5 μM carfilzomib (Cfzb) for 48 hrs. P value: two-tailed t-test; n = 3. **L.**
604 Autophagy assay for iPSC-CMs treated with 0 (Ctrl) vs. 0.5 μM carfilzomib (Cfzb) for 48 hrs, and
605 positive control (Pos); data were normalized to DAPI and normal cells. P value: two-tailed t-test; n =
606 10. **M.** log2 Turnover rate ratios between carfilzomib-treated and untreated iPSC-CM from the
607 spatiotemporal proteomics data. Proteins assigned the proteasome compartment have significantly
608 increased temporal kinetics; proteins in the lysosome/junction and chromatin/sarcomere
609 compartments have significantly reduced temporal kinetics. P values: Mann-Whitney; with a threshold
610 of 0.05/14 considered significant. Center line: median; box limits: interquartile range; whiskers: 1.5x
611 interquartile range.

612 Among proteins with spatial information, we compared the temporal kinetics of 2,648
613 proteins. Unexpectedly, there was no overall slowdown of protein temporal kinetics with the
614 median protein half-lives being 97.4 hours and 100.0 hours in normal and carfilzomib-treated
615 cells, respectively (**Figure 6J**; **Supplemental Data S8**), suggesting that at 48 hours following
616 proteasome inhibitor treatment, the observed cellular toxicity is not directly explainable by a
617 drop of per-protein average in global protein degradation. At 48 hours of carfilzomib
618 treatment in iPSC-CMs, proteasome chymotrypsin-like activities are partially suppressed but
619 significant partial activities are also observable (**Figure 6K**); whereas other proteolysis
620 mechanisms may also compensate for proteasome inhibition, including a suggestive increase
621 in autophagy (P: 0.053) (**Figure 6L**). Inspection of the spatial data revealed that the changes
622 in protein kinetics upon carfilzomib are localization specific, with a significant reduction in
623 chromatin/sarcomere protein turnover rate, and significant increase for the proteasome
624 compartment under carfilzomib treatment (**Figure 6M**).
625 Notably, on an individual protein level we find that the majority of proteins with
626 increased protein kinetics belong to subunits of the regulatory 19S complex rather than the
627 core 20S complex (**Figure 7A**) suggesting possible changes in 26S proteasome activity and
628 target engagement. In addition to proteasome subunits, the temporal kinetics revealed a
629 robust induction of chaperons HSP90AA1/HSP90A, HSP90AB1/HSP90B, HSPA4, and BAG3;
630 and ERAD associated proteins VCP and UFD1 (**Figure 7B, Supplemental Data S8**). Within
631 the mitochondrion, quality control proteins HSPD1, HSPE1, and CLPB are induced (**Figure**
632 **7A**). In contrast, among proteins that show reduced turnover in carfilzomib treatment are
633 major sarcomeric proteins MYH6, MYH7, MYBPC3, MYL7; as well as proteins classified to the
634 cell junction compartment dystrophin (DMD) and utrophin (UTRN), and the desmosome
635 complex protein desmoplakin (DSP) (**Figure 7A & C**).

636 We observed an interconnectivity of spatial and temporal changes, with 23 out of 339
637 pairs of confident translocators also showing significant kinetic changes. BAG3, a muscle
638 chaperone important for sarcomere turnover (Martin et al., 2021a), shows elevated kinetics
639 (**Figure 7B**) and a partition away from the soluble cytosol compartment (**Figure 7D**) toward
640 an expanded compartment in carfilzomib that co-sediments with Golgi markers. Inspection
641 of existing annotations show that the majority of categorized proteins are not canonical Golgi
642 proteins but contain cytoplasm and endosome terms; hence it likely represents a less soluble
643 cytoplasmic fraction consistent with a lower abundance in the last ultracentrifugation step
644 (**Supplemental Figure S13**, **Supplemental Figure S14, Supplemental Data S9**). This is
645 consistent with the known dynamic partitioning of BAG3 between the cytosol and
646 myofilament fractions for its function (Martin et al., 2021b). Secondly, we find that
647 accelerated temporal kinetics of PA200/PSME4 proteasome activator (**Figure 7B**) in
648 conjunction with a change in localization from the nuclear compartment in baseline toward
649 the proteasome compartment upon carfilzomib (**Figure 7E**). The PSME4/PA200 proteasome
650 activator is known to bind with the 20S/26S proteasome complex to stimulate proteolysis and
651 has a putative nuclear localization signal (Ustrell et al., 2002). The change in localization is
652 therefore consistent with increased binding with the proteasome complex. In parallel, the
653 proteasome activator PA28/PSME3 also relocalizes to the proteasome upon carfilzomib
654 (**Supplemental Figure S15**), altogether suggesting a remodeling of proteasome configuration
655 upon carfilzomib.
656 Taken together, the spatiotemporal proteomics data here identified major
657 proteostatic pathways induced in carfilzomib, involving a potential remodeling of the
658 proteasome, induction of chaperones and ERAD proteins, and mitochondrial protein quality
659 control mechanisms that may be important for preserving function. On the other hand, a
660 preferential decrease of temporal kinetics in sarcomere and desmosome proteins suggest
661 that the interruption of protein quality control and turnover in these important cardiomyocyte
662 components may be principal sites of lesion in carfilzomib cardiotoxicity. Finally, we
663 assessed the protein-level expression profiles in the hearts of mice treated with carfilzomib
664 for 2 weeks to model cardiac dysfunction (Supplemental Methods). Notably, we find
665 differential protein abundance analysis showed that MHC-β (MYH7) and desmoplakin (DSP)
666 are the 1st and 5th most significantly up-regulated proteins among 3,379 quantified proteins
667 in the hearts of mice treated with carfilzomib (**Supplemental Figure S16**), consistent with
668 their accumulation following proteasome inhibition and suggesting the possibility that
669 similar proteostatic lesions may underlie cardiotoxicity mechanism in vivo.

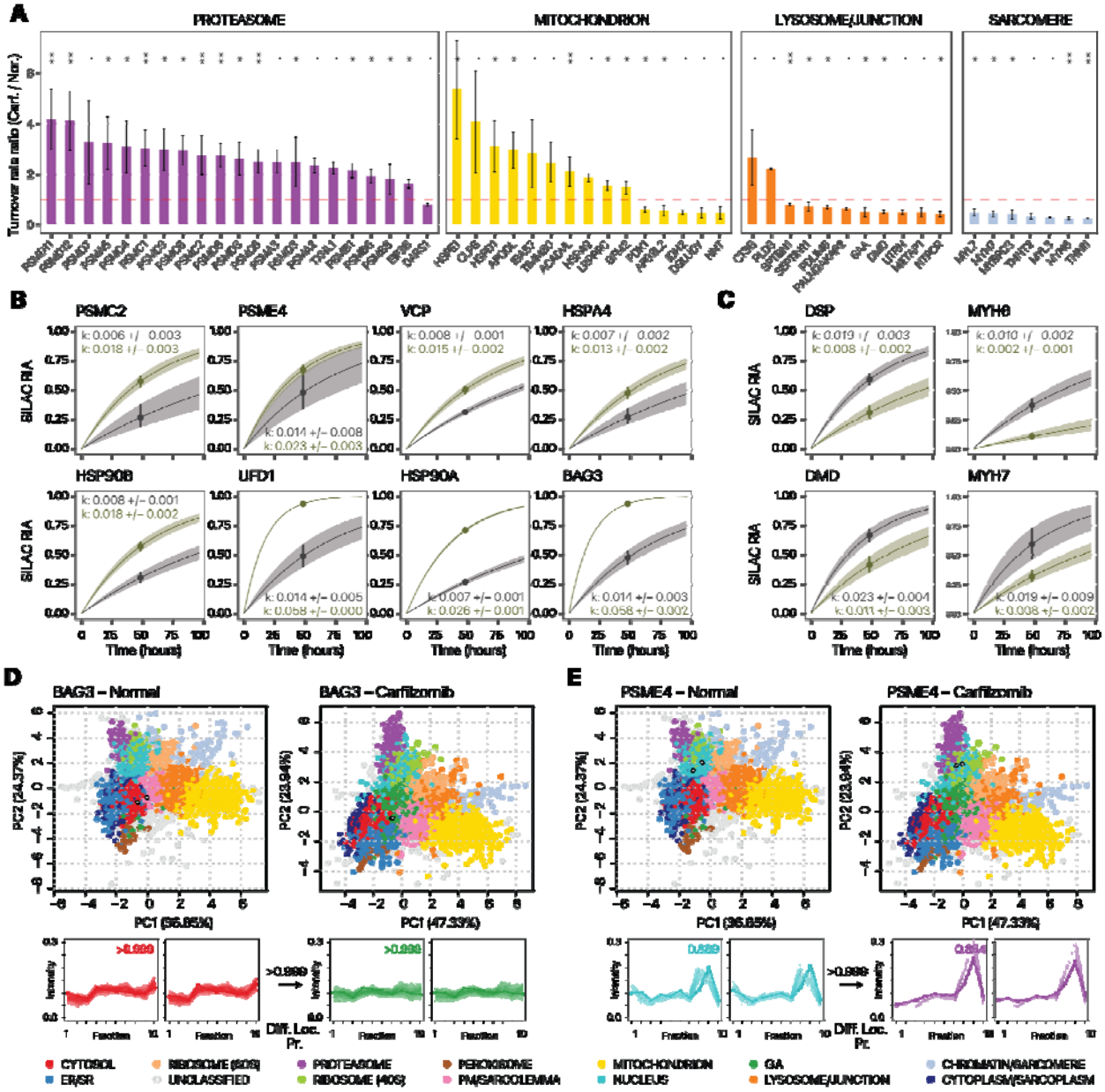

Figure 7. Proteostatic pathways and lesions in carfilzomib mediated cardiotoxicity in iPSC-CMs. **A.** Changes in protein turnover rates between carfilzomib vs. normal iPSC-CMs across selected cellular compartments; **: P < 0. 01; *: P < 0.05; .: P < 0.1; Mann-Whitney test FDR adjusted P values. error bars: standard error. **B.** Kinetic curve representations of proteins with accelerated temporal kinetics in carfilzomib including PSMC2 which corresponds to the ratio in panel A, as well as additional ERAD proteins and chaperones; gray: normal iPSC-CM; green: carfilzomib. **C.** Kinetic curve representations of slowdown of protein kinetics in DSP, DMD, MYH6, and MYH7, corresponding to the ratios in panel A. **D–E.** Spatial map (PC1 vs. PC2) and ultracentrifugation fraction profiles of **D.** BAG3 and **E.** PSME4 in normal and carfilzomib-treated human iPSC-CM, showing a likely differential localisation in conjunction with kinetics changes. White-filled circles: light and heavy BAG3 or PSME4 in each plot. The kinetic curves of BAG3 and PSME4 are in panel B. Numbers at arrows correspond to BANDLE differential localization probability (Diff. Loc. Pr.).

683 # Discussion

684 Advances in spatial proteomics have opened new avenues to discover the subcellular
685 localization of proteins on a proteome scale. Thus far however, few efforts have linked the
686 spatial dynamics of the proteome to other dynamic proteome parameters, which hinders a
687 multi-dimensional view of protein function (Burnum-Johnson et al., 2022; Larance et al.,
688 2013). Co-labeling of SILAC (MS1) and TMT (MS2) tags have been used to increase the
689 channel capacity of quantitative proteomics experiments (Dephoure and Gygi, 2012). Here
690 we adopted the extended labeling capacity to encode spatial and temporal information in the
691 same experiment (**Figure 1D**). The SPLAT design has the advantages of resolving proteome-
692 wide temporal kinetics and spatial distributions in the same experiments and identifying
693 their interactions such as compartment-specific turnover; secondly, it allows separate
694 observations of spatial distribution of new vs. old protein pools. Despite each of the SILAC
695 labeled pairs (light and heavy) and their associated TMT profiles being separately quantified
696 by mass spectrometry as independent ions, the spatial profiles of light and heavy proteins
697 are highly similar under baseline conditions (**Figure 4A-B**) which provides additional
698 assurance of spatial assignments.

699 Applying the workflow to human AC16 cardiac cells under thapsigargin and
700 tunicamycin induced ER stress and the associated UPR, we observed that both ER stress
701 inducing drugs led to a global suppression in turnover rate, consistent with the reduced
702 translation known to be caused by ER stress. The temporal kinetics data of individual
703 proteins revealed the coordinated activation of known and suspected stress mediators
704 through their increased kinetics, particularly concentrated in the ER and Golgi compartments
705 (**Figure 2E**). At the same time, the spatial proteomics profiles revealed substantial
706 endomembrane remodeling and hundreds of translocating proteins under ER stress. A recent
707 work also reported ~75 translocator protein candidates under acute low-dose thapsigargin
708 (250 nM for 1 hr) in U-2 OS cells, although the experimental approach was more optimized
709 toward mRNA detection (Villanueva et al., 2022). The spatial data here add to an emerging
710 view of dynamical protein regulation under cellular stress, illustrating a differential
711 localization of RNA binding proteins to stress granules, targeting of specific proteins toward
712 lysosomes, as well as membrane trafficking of ion channels and amino acid transporters.
713 UPR activation is known to induce the biosynthesis of non-essential or partly-essential amino
714 acids despite protein synthesis suppression (Gonen et al., 2019); the recycling of lysosomal
715 lysine and arginine regulates the sensitivity to ER stress (Higuchi-Sanabria et al., 2020);
716 whereas deprivation of amino acids is known to activate downstream pathways of UPR
717 including CHOP in vitro (Harding et al., 2003). Moreover, the knockdown of SLC3A2 has been
718 found to suppress the activation of ER stress response pathways including ATF4/6 induction
719 (Liu et al., 2018), together suggesting amino acid transporters may function in ER stress
720 response. The data here indicate that these transporters may in turn be regulated by their
721 spatial localization beyond steady-state abundance. Other changes are found that may be
722 specific to stressors. Tunicamycin treatment leads to a further decrease in turnover of
723 lysosomal proteins compared to other organelles. The lysosome plays important roles in
724 recycling of glycans, a process which may be slowed under ER stress in response to the
725 decrease in glycosylation.

726 Changes in protein spatial distribution can occur due to a relocation of an existing
727 protein, where in a protein may respond to a signaling cue such as a post-translational
728 modification status and subsequently migrate to a subcellular location. Alternatively, an
729 alternate localization of newly synthesized proteins can also drive spatial redistribution. By
730 comparing the translocation behaviors of new and old protein pools separately, we were able
731 to observe a partitioning of new and old protein pools including epidermal growth factor
732 receptor (EGFR/ErbB1/HER1). ErbB family proteins are required for both normal heart
733 development and prevention of cardiomyopathies in the adult heart. EGFR is a receptor
734 tyrosine kinase of this family capable of triggering multiple signaling cascades, and can be
735 activated via both ligand dependent and ligand independent pathways. Upon ER stress
736 induction, EGFR immunofluorescence showed a partial translocation away from the plasma
737 membrane. Although immunofluorescence cannot distinguish between old and new protein
738 pools, this partial translocation is consistent with the mass spectrometry data showing
739 partial translocation, involving the newly synthesized heavy protein pool. We hypothesize
740 that this partial translocation is suggestive of a ligand-independent trafficking of newly
741 synthesized protein, rather than ligand dependent activation and internalization that is
742 agnostic to protein lifetime. Of note, ligand-independent activation and internalization of
743 EGFR has been previously induced via both starvation and tyrosine kinase inhibitor
744 treatment, leading to cellular autophagy (Tan et al., 2015), hence this partial translocation
745 may carry functional significance to protective cellular response.
746 We further applied SPLAT to a different, non-proliferating cell type, namely human
747 iPSC-derived cardiomyocytes, which have gained increasing utility for modeling the
748 cardiotoxic effects of the cancer drugs, including carfilzomib. In the carfilzomib experiment,
749 the data from SPLAT revealed a surprising similarity in global turnover rates between control
750 and treatment. These observations are consistent with a compensatory rescue of proteasome
751 abundance and activity previously observed in proteasome inhibition by carfilzomib (Demo
752 et al., 2007; Forghani et al., 2021) or bortezomib (Meiners et al., 2003) in other cell types.
753 Proteasomes are known to be regulated by negative feedback mechanisms (Meiners et al.,
754 2003; Xie and Varshavsky, 2001; Xu et al., 2008), which could explain the lack of change in
755 proteome-wide half-life differences and instead suggest that toxicity may derive from more
756 specific cellular lesions. We identified a significant reduction in turnover in sarcomere
757 proteins, which may be particularly sensitive to interruptions in proteasome activity and
758 moreover may account for the bulk of turnover flux in iPSC-CMs given their high abundance.
759 Finally, the activation and translocation of proteostatic pathway proteins BAG3 and
760 PA200/PSME4 in cardiac cells may be explored as potential targets to ameliorate
761 proteostatic disruptions and cardiotoxic effects.

762 **Limitations**

763 Although there is no inherent limit to the number of dynamic SILAC labeling time points that
764 can be investigated, in our experiments we have used only a single time point per treatment
765 (16 hours post thapsigargin or tunicamycin; 48 hours post carfilzomib), which was selected
766 based on the drug treatment models but also needed to be sufficient to capture the median
767 half-life of proteins in the cell types studied (**Figure 2D; Figure 6J**). Hence the collection time

768 points need to be optimized for different cell types with distinct intrinsic protein turnover
769 rates. Synthesized proteins may have further relocalized following the start of dynamic
770 SILAC labeling, hence some acute translocation responses may be missed. Although the
771 inclusion of earlier time points might provide insight into early translocation events, reaching
772 this objective may be technically challenging, as the acquisition of spatial localization
773 information from the heavy SILAC labeled peptides would be hindered by their low intensity.
774 The double labeling design also requires independent MS2 acquisition of light and heavy
775 peptides, which can decrease the depth and data completeness of mass spectrometry-based
776 proteomics analysis. Future work may alleviate this limitation by modifying the mass
777 spectrometry acquisition methods to automatically trigger the acquisition of heavy peptides
778 and reduce incomplete light-heavy pairs.

779 Secondly, SPLAT shares limitations that are common to common spatial proteomics
780 strategies. The differential ultracentrifugation method employed here requires $\sim 10^7$ cells and
781 cannot resolve some subcellular fractions, e.g., lysosome from cell junction. The number of
782 classifiable subcellular localizations here is in line with other LOPIT-DC studies, and may be
783 improved in future work that attempts to couple turnover analysis to gradient-based
784 sedimentation approaches with higher spatial resolution. Protein correlation profiling based
785 techniques generally face challenges in recognizing proteins with multiple localizations or
786 partial translocations. For instance, the multi-functional ERAD protein p97/VCP is known to
787 have multiple subcellular localizations, but its precise subcellular translocation profile is
788 difficult to interpret from the TMT data and is unclassified to any compartment. Because
789 translocation may be sub-stoichiometric, translocated proteins can have lower confidence in
790 classification of location. Hence, other biologically relevant translocators reside in the data
791 that await exploration. In the thapsigargin and tunicamycin experiments, upward of 1,000
792 candidate translocation patterns were detected with significant differences in localization
793 (99% probability) using BANDLE, but many proteins presented a challenge to clear
794 interpretation of compartments upon manual inspection. Progress in this area may require
795 development of spatial separation methods that combine orthogonal separation principles.

796 In summary, we describe an experimental workflow and data analysis pipeline that
797 integrates dynamic time-resolved stable isotope labeling kinetic analysis with differential
798 ultracentrifugation-based subcellular proteomics to characterize proteome-wide spatial and
799 temporal changes upon perturbation. This method may be broadly useful for understanding
800 the function and behaviors of proteins inside the cell, and may provide new insight into the
801 mechanisms that regulate protein stability and localization in stress, disease, and drug
802 treatment.

803 Methods

804 Additional methods can be found in the Supplemental Information file.

805 AC16 Cell culture, metabolic labeling, UPR induction

806 AC16 cells procured from Millipore between passage number 11 and 16 were cultured in
807 DMEM/F12 supplemented with 10% FBS and no antibiotics. Cells were maintained at 37°C

808 with 5% CO_2 and 10% O_2. For isotopic labeling, SILAC DMEM/F12 (Thermo Scientific)
809 deficient in both L-lysine and L-arginine was supplemented with 1% dialyzed FBS and heavy
810 amino acids $^{13}C_6{}^{15}N_2$ L-Lysine-2HCl and $^{13}C_6{}^{15}N_4$ L-Arginine-HCl (Thermo Scientific) at
811 concentrations of 0.499 mM and 0.699 mM, respectively. Light media was switched to heavy
812 media and cells were labeled for 16 hours prior to harvest. UPR was induced with 1 μM
813 thapsigargin (SelleckChem) or 1 μg/mL tunicamycin (Sigma) at the same time as isotopic
814 labeling.

815 **Cell harvest, differential centrifugation, and isobaric labeling**

816 Cell harvest and subcellular fractionation was performed based on the LOPIT-DC differential
817 ultracentrifugation protocol as described in Geladaki et al. (Geladaki et al., 2019). Briefly,
818 AC16 cells were treated, harvested with trypsinization, washed 3× with room temperature
819 PBS, and resuspended in a detergent free gentle lysis buffer (0.25 M sucrose, 10 mM HEPES
820 pH 7.5, 2 mM magnesium acetate). 1.5 mL of suspension at a time was lysed using an
821 Isobiotec ball bearing homogenizer with a 16 μM clearance size until ~80% of cell
822 membranes were lysed, as verified with trypan blue (approximately 15 passes through the
823 chamber). Lysates were spun 3 times each in a 4°C swinging bucket centrifuge 200 × g, 5
824 min to remove unlysed cells. The supernatant was retained and used to generate the 9
825 ultracentrifugation pellets using spin parameters shown in **Supplemental Table S2.**

826 The supernatant generated in the final spin was removed and all pellets and the final
827 supernatant were stored at -80°C until proceeding. Supernatant was thawed on ice and
828 precipitated in 3× the volume of cold acetone overnight at –20°C.This was used to generate
829 pellet 10 by centrifuging at 13,000 × g for 10 minutes at 4°C. Excess acetone was removed
830 and the pellet was allowed to dry briefly before resuspension in a resolubilization buffer of 8
831 M urea, 50 mM HEPES pH 8.5, and 0.5% SDS with 1x Halt Protease and Phosphatase Inhibitor
832 Cocktail (Thermo Scientific). The suspension was sonicated in a Biorupter with settings 20×
833 30s on 30s off at 4°C.

834 Pellets from the ultracentrifugation fractions 1 to 9 were resuspended in RIPA buffer with
835 Halt Protease and Phosphatase Inhibitor Cocktail (Thermo Scientific) with sonication in a
836 Biorupter with settings 10x 30s on 30s off at 4°C. Insoluble debris was removed from all
837 samples (1-10) by centrifugation at 14,000 × g, 5 minutes. Protein concentration of all
838 samples was measured with Rapid Gold BCA (Thermo Scientific). The samples were
839 digested and isobarically tagged using the iFASP protocol (McDowell et al., 2013). 25 ug
840 protein per sample in 250 uL 8M urea was loaded onto Pierce Protein Concentrators PES, 10K
841 MWCO prewashed with 100 mM TEAB. The samples were again washed with 8 M urea to
842 denature proteins and remove SDS. The samples were washed with 300 uL 100 mM TEAB
843 twice. The samples were then reduced and alkylated with TCEP and CAA for 30 minutes at
844 37°C in the dark. CAA and TCEP were removed with centrifugation and the samples were
845 washed 3x with 100 mM TEAB. Samples were digested atop the filters overnight at 37°C
846 with mass spectrometry grade trypsin (Promega) at a ratio of 1:50 enzyme:protein. A total of
847 0.2 mg of TMT-10plex isobaric labels (Thermo Scientific) per differential centrifugation

848 fraction were equilibrated to room temperature and reconstituted in 20 μL LC-MS grade
849 anhydrous acetonitrile. In each experiment, labels were randomly assigned to each fraction
850 (**Supplemental Tables S3-S4**) with a random number generator to mitigate possible batch
851 effect. Isobaric tags were added to peptides still atop the centrifugation filters and incubated
852 at room temperature for 1 hour with shaking. The reactions were quenched with 1 μL 5%
853 hydroxylamine at room temperature for 30 minutes with shaking. Labeled peptides were
854 eluted from the filters with centrifugation. To further elute labeled peptides 40 μL 50 mM
855 TEAB was added and filters were again centrifuged. All 10 labeled fractions per experiment
856 were combined and mixed well before dividing each experiment into two aliquots. Aliquots
857 were dried with speed-vac and stored at –80°C.

858 **Liquid chromatography and mass spectrometry**

859 One aliquot per experiment was reconstituted in 50 μL 20 mM ammonium formate pH 10 in
860 LC-MS grade water (solvent A) for high pH reverse phase liquid chromatography (RPLC)
861 fractionation. The entire sample was injected into a Jupiter 4 μm Proteo 90 Å LC Column of
862 150 $\times$ 1 mm on a Ultimate 3000 HPLC system. The gradient was run with a flow rate of 0.1
863 mL/min as follows: 0–30 min: 0%–40% Solvent B (20 mM ammonium formate pH 10 in 80% LC-
864 MS grade acetonitrile); 30–40 min: 40%-80% Solvent B; 40–50 min: 80% Solvent B. Fractions
865 were collected every minute and pooled into a total of 20 peptide fractions, then dried with
866 speed-vac.
867 The dried fractions were reconstituted in 10 μL each of pH 2 MS solvent A (0.1%
868 formic acid) and analyzed with LC-MS/MS on a Q-Exactive HF orbitrap mass spectrometer
869 coupled to an LC with electrospray ionization source. Peptides were separated with a
870 PepMap RSLC C18 column 75 μm x 15 cm, 3 μm particle size (ThermoScientific) with a 90
871 minute gradient from 0 to 100% pH 2 MS solvent B (0.1% formic acid in 80% LC-MS grade
872 acetonitrile). Full MS scans were acquired with a 60,000 resolution. A stepped collision
873 energy of 27, 30 and 32 was used and MS2 scans were acquired with a 60,000 resolution and
874 an isolation window of 0.7 m/z.

875 **Mass spectrometry data processing and turnover analysis**

876 Mass spectrometry raw data were converted to mzML format using ThermoRawFileParser
877 v.1.2.0 (Hulstaert et al., 2020) then searched against the UniProt Swiss-Prot human canonical
878 and isoform protein sequence database (retrieved 2022-10-27) using Comet v.2020_01_rev3
879 (Eng et al., 2015). The fasta database was further appended with contaminant proteins using
880 Philosopher v4.4.0 (total 42,402 forward entries). The search settings were as follows:
881 peptide mass tolerance: 10 ppm; isotope error: 0/1/2/3; number of enzyme termini: 1; allowed
882 missed cleavages: 2; fragment bin tolerance: 0.02; fragment bin offset: 0; variable
883 modifications: TMT-10plex tag +229.1629 for TMT experiments, and lysine + 8.0142, arginine
884 + 10.0083 for all SILAC experiments; fixed modifications: cysteine + 57.0214. The search
885 results were further reranked and filtered using Percolator v3.0 (The et al., 2016) at a 5% FDR.
886 Following database search, the mzML files and Percolator PSMs were input to the SPLAT
887 pipeline. The dynamic SILAC data were analyzed using RIANA v0.7.1 (Hammond et al., 2022)

888 to integrate the peak intensity within a 25 ppm error of the light (+0), heavy (+8, +10), and
889 double K/R (+16, +18, +20) peptide peaks over a 20 second retention time window
890 encompassing the first and last MS2 scan where the peptide is confidently identified. We
891 then calculated the fractional synthesis of all K/R containing peptides as the intensity of the
892 0th isotopomer peak (m0) over the sum of applicable light and heavy isotopomers (e.g.,
893 m0/m0+m8 for a peptide with one lysine). RIANA then performs intensity-weighted least-
894 square curve-fitting using the scipy optimize function to a first-order exponential rise model
895 to find the best-fit peptide turnover rate. Protein turnover rates are calculated as the
896 harmonic mean of peptide turnover rates

897 **Subcellular localization classification**

898 Subcellular localization classification and translocation predictions were performed using the
899 pRoloc (Gatto et al., 2014) and the BANDLE (Crook et al., 2022) packages in R/Bioconductor.
900 Three replicate batches of AC16 cells per condition each were individually labeled and
901 treated, fractionated and analyzed by mass spectrometry, and biological replicate data were
902 used for pRoloc and BANDLE analysis. Briefly, the subcellular localization markers were
903 selected from the intersecting proteins with a prior data set generated from human U-2 OS
904 osteosarcoma cells (Geladaki et al., 2019) with further curation to account for cell type
905 specific marker expression (**Supplemental Data S10**). A random walk algorithm is used to
906 prune the markers to maximize normalized between-class separation. For differential
907 localization analyses we used the Markov-chain Monte-Carlo (MCMC) and non-parametric
908 model in BANDLE to find unknown protein classification and evaluate differential
909 localization probability. MCMC parameters are 9 chains, 10,000 iterations, and 5,000 burn-in,
910 20 thinning, seed 42; convergence of the Markov chains is assessed visually by rank plots as
911 recommended (Crook et al., 2019). For additional analysis to describe baseline protein
912 classification and compare MS2 and MS3 performance, a T-augmented Gaussian mixture
913 model with a maximum a posteriori (MAP) method in pRoloc was used.

914 **Human iPSC-derived cardiomyocytes and proteasome inhibition**

915 Human AICS-0052-003 induced pluripotent stem cell (iPSC) (mono-allelic C-terminus mEGFP-
916 tagged MYL7 WTC; Allen Institute Cell Collection) line was acquired from Coriell Institute
917 and seeded onto Geltrex (Gibco) coated 6 well plates and maintained in StemFlex (Thermo
918 Scientific) media at 37 °C, 5% CO2 with daily media changes. At 80% confluency, cells were
919 passaged using 0.5 mM EDTA before resuspension in StemFlex supplemented with 10 μM Y-
920 27632 (Selleck). Cells were replated into Geltrex coated 12 well plates at a density of 3×10^5
921 cells/well and daily media changes of StemFlex continued until the cells reached 80%
922 confluency, day 0 of cardiac differentiation. The iPSCs were differentiated into
923 cardiomyocytes using a small molecule based GSK-3 inhibition-Wnt inhibition protocol
924 (Burridge et al., 2014). Briefly, on day 0, cell media was replaced with 2 mL/well RPMI
925 supplemented with B-27 minus insulin (Gibco) and 6 □M CHIR99021 (STEMCELL); on day 2,
926 the media was changed to 2 mL/well RPMI+B-27 minus insulin. On day 3, the media was
927 changed to 2 mL/well RPMI+B27 minus insulin supplemented with 5 □M IWR-1-Endo

928 (STEMCELL). On day 7, the media was changed to 2 mL RPMI+B27 with insulin.
929 Differentiation was confirmed via visualization of morphology, spontaneous contraction of
930 cells, and imaging of the GFP tagged MYL7/MLC-2a. On day 9, the media was changed to
931 RPMI+B27 with insulin without glucose to select for cardiomyocytes. The cardiomyocytes
932 were then passaged at low density with 2 μM CHIR-99021 (Maas et al., 2021). At
933 approximately 75% confluency on passage 2, CHIR supplemented media was removed and
934 replaced with RPMI B-27 with insulin, and used for experiments on day 25–30 post
935 differentiation. For isotopic labeling, RPMI (Thermo Scientific) deficient in both L-lysine and
936 L-arginine was supplemented with B27 with insulin and heavy amino acids $^{13}C_6{}^{15}N_2$ L-Lysine-
937 2HCl and $^{13}C_6{}^{15}N_4$ L-Arginine-HCl (Thermo Scientific) at concentrations 0.219 mM and 1.149
938 mM, respectively. 48 hours after CHIR removal, light media was replaced with this heavy
939 media and cells were labeled for 48 hours prior to harvest. 0.5 μM carfilzomib (Selleck) was
940 added with heavy media in the treatment group. Harvesting and ultracentrifugation
941 proceeded as above with the following exception. Due to the diffuse nature of pellets
942 generated in the iPSC-derived cardiomyocytes (iPSC-CM) control experiment, the MLA-50
943 (Beckman) rotor was switched to the TLA-55 rotor after generation of pellet 5. Consistent
944 force (g) of each spin was maintained by increasing the smaller rotor's RPM on subsequent
945 spins. This change was repeated during the iPSC-CM treatment experiment. Proteins from
946 each cellular fraction were digested and analyzed with mass spectrometry as above.

947 Data Availability

948 Raw mass spectrometry data have been uploaded to ProteomeXchange under the accession
949 numbers PXD038054, PXD041386, PXD046669, PXD046670, and PXD046671. Source data are
950 provided with this paper.

951 Code Availability

952 Software code for the SPLAT pipeline is available on GitHub at https://github.com/lau-
953 lab/splat, https://github.com/ed-lau/riana and https://github.com/ed-lau/pytmt.
954

955 Author Contributions

956 J.C. and E.L. conceptualized the study. J.C., V.M., S.K.R. V.H., C.L., V.A., R.W.L., K.Z., J.P., J-
957 W.R. and M.P.L. performed experiments. J.C., V.M., and E.L. processed the data and
958 interpreted the results. J.C. and E.L. wrote software code and performed analysis. J.C.,
959 S.K.R., V.M., and E.L. drafted and revised the manuscript. J-W.R., Z.V.W., M.P.L., and E.L.
960 managed funding. All authors read and approved the final version of the manuscript.

961 Acknowledgments

962 The authors thank Dr. Christopher Ebmeier (Director, Proteomics and Mass Spectrometry
963 Core Facility, University of Colorado Boulder) for his assistance with TMT-MS3 experiments.

964 This work was supported in part by NIH award K08-HL148540 to J-W.R., NIH awards R01-
965 HL141278 and R01-GM144456 to M.P.L. and NIH awards R35-GM146815 to E.L; and the
966 University of Colorado SOM Translational Research Scholars Program (TSRP) award to E.L..

967 ## References

968 Andrews, B., Murphy, A.E., Stofella, M., Maslen, S., Almeida-Souza, L., Skehel, J.M., Skene,
969 N.G., Sobott, F., Frank, R.A.W., 2022. Multidimensional Dynamics of the Proteome in
970 the Neurodegenerative and Aging Mammalian Brain. Mol. Cell. Proteomics 21,
971 100192. https://doi.org/10.1016/j.mcpro.2021.100192
972 Bresson, S., Shchepachev, V., Spanos, C., Turowski, T.W., Rappsilber, J., Tollervey, D., 2020.
973 Stress-Induced Translation Inhibition through Rapid Displacement of Scanning
974 Initiation Factors. Mol. Cell 80, 470-484.e8.
975 https://doi.org/10.1016/j.molcel.2020.09.021
976 Burnum-Johnson, K.E., Conrads, T.P., Drake, R.R., Herr, A.E., Iyengar, R., Kelly, R.T.,
977 Lundberg, E., MacCoss, M.J., Naba, A., Nolan, G.P., Pevzner, P.A., Rodland, K.D.,
978 Sechi, S., Slavov, N., Spraggins, J.M., Van Eyk, J.E., Vidal, M., Vogel, C., Walt, D.R.,
979 Kelleher, N.L., 2022. New Views of Old Proteins: Clarifying the Enigmatic Proteome.
980 Mol. Cell. Proteomics 21, 100254. https://doi.org/10.1016/j.mcpro.2022.100254
981 Burridge, P.W., Matsa, E., Shukla, P., Lin, Z.C., Churko, J.M., Ebert, A.D., Lan, F., Diecke, S.,
982 Huber, B., Mordwinkin, N.M., Plews, J.R., Abilez, O.J., Cui, B., Gold, J.D., Wu, J.C.,
983 2014. Chemically defined generation of human cardiomyocytes. Nat. Methods 11, 855–
984 860. https://doi.org/10.1038/nmeth.2999
985 Chartron, J.W., Hunt, K.C.L., Frydman, J., 2016. Cotranslational signal-independent SRP
986 preloading during membrane targeting. Nature 536, 224–228.
987 https://doi.org/10.1038/nature19309
988 Christopher, J.A., Stadler, C., Martin, C.E., Morgenstern, M., Pan, Y., Betsinger, C.N., Rattray,
989 D.G., Mahdessian, D., Gingras, A.-C., Warscheid, B., Lehtiö, J., Cristea, I.M., Foster,
990 L.J., Emili, A., Lilley, K.S., 2021. Subcellular proteomics. Nat. Rev. Methods Primer 1,
991 32. https://doi.org/10.1038/s43586-021-00029-y
992 Claydon, A.J., Beynon, R., 2012. Proteome dynamics: revisiting turnover with a global
993 perspective. Mol. Cell. Proteomics MCP 11, 1551–1565.
994 https://doi.org/10.1074/mcp.O112.022186
995 Cromm, P.M., Crews, C.M., 2017. The Proteasome in Modern Drug Discovery: Second Life of a
996 Highly Valuable Drug Target. ACS Cent. Sci. 3, 830–838.
997 https://doi.org/10.1021/acscentsci.7b00252
998 Crook, O.M., Breckels, L.M., Lilley, K.S., Kirk, P.D.W., Gatto, L., 2019. A Bioconductor
999 workflow for the Bayesian analysis of spatial proteomics. F1000Research 8, 446.
1000 https://doi.org/10.12688/f1000research.18636.1
1001 Crook, O.M., Davies, C.T.R., Breckels, L.M., Christopher, J.A., Gatto, L., Kirk, P.D.W., Lilley,
1002 K.S., 2022. Inferring differential subcellular localisation in comparative spatial
1003 proteomics using BANDLE. Nat. Commun. 13, 5948. https://doi.org/10.1038/s41467-
1004 022-33570-9
1005 Crook, O.M., Mulvey, C.M., Kirk, P.D.W., Lilley, K.S., Gatto, L., 2018. A Bayesian mixture
1006 modelling approach for spatial proteomics. PLOS Comput. Biol. 14, e1006516.
1007 https://doi.org/10.1371/journal.pcbi.1006516
1008 Demo, S.D., Kirk, C.J., Aujay, M.A., Buchholz, T.J., Dajee, M., Ho, M.N., Jiang, J., Laidig, G.J.,
1009 Lewis, E.R., Parlati, F., Shenk, K.D., Smyth, M.S., Sun, C.M., Vallone, M.K., Woo, T.M.,
1010 Molineaux, C.J., Bennett, M.K., 2007. Antitumor Activity of PR-171, a Novel

1011 Irreversible Inhibitor of the Proteasome. Cancer Res. 67, 6383–6391.
1012 https://doi.org/10.1158/0008-5472.CAN-06-4086
1013 Dephoure, N., Gygi, S.P., 2012. Hyperplexing: A Method for Higher-Order Multiplexed
1014 Quantitative Proteomics Provides a Map of the Dynamic Response to Rapamycin in
1015 Yeast. Sci. Signal. 5. https://doi.org/10.1126/scisignal.2002548
1016 Doherty, M.K., Hammond, D.E., Clague, M.J., Gaskell, S.J., Beynon, R.J., 2009. Turnover of the
1017 human proteome: determination of protein intracellular stability by dynamic SILAC. J.
1018 Proteome Res. 8, 104–112. https://doi.org/10.1021/pr800641v
1019 Dostal, V., Wood, S.D., Thomas, C.T., Han, Y., Lau, E., Lam, M.P.Y., 2020. Proteomic
1020 signatures of acute oxidative stress response to paraquat in the mouse heart. Sci.
1021 Rep. 10, 18440. https://doi.org/10.1038/s41598-020-75505-8
1022 Eng, J.K., Hoopmann, M.R., Jahan, T.A., Egertson, J.D., Noble, W.S., MacCoss, M.J., 2015. A
1023 deeper look into Comet--implementation and features. J. Am. Soc. Mass Spectrom. 26,
1024 1865–1874. https://doi.org/10.1007/s13361-015-1179-x
1025 Forghani, P., Rashid, A., Sun, F., Liu, R., Li, D., Lee, M.R., Hwang, H., Maxwell, J.T.,
1026 Mandawat, A., Wu, R., Salaita, K., Xu, C., 2021. Carfilzomib Treatment Causes
1027 Molecular and Functional Alterations of Human Induced Pluripotent Stem Cell–
1028 Derived Cardiomyocytes. J. Am. Heart Assoc. 10, e022247.
1029 https://doi.org/10.1161/JAHA.121.022247
1030 Fridolfsson, H.N., Kawaraguchi, Y., Ali, S.S., Panneerselvam, M., Niesman, I.R., Finley, J.C.,
1031 Kellerhals, S.E., Migita, M.Y., Okada, H., Moreno, A.L., Jennings, M., Kidd, M.W.,
1032 Bonds, J.A., Balijepalli, R.C., Ross, R.S., Patel, P.M., Miyanohara, A., Chen, Q.,
1033 Lesnefsky, E.J., Head, B.P., Roth, D.M., Insel, P.A., Patel, H.H., 2012. Mitochondria-
1034 localized caveolin in adaptation to cellular stress and injury. FASEB J. Off. Publ. Fed.
1035 Am. Soc. Exp. Biol. 26, 4637–4649. https://doi.org/10.1096/fj.12-215798
1036 Gatto, L., Breckels, L.M., Wieczorek, S., Burger, T., Lilley, K.S., 2014. Mass-spectrometry-
1037 based spatial proteomics data analysis using pRoloc and pRolocdata. Bioinformatics
1038 30, 1322–1324. https://doi.org/10.1093/bioinformatics/btu013
1039 Geladaki, A., Kočevar Britovšek, N., Breckels, L.M., Smith, T.S., Vennard, O.L., Mulvey, C.M.,
1040 Crook, O.M., Gatto, L., Lilley, K.S., 2019. Combining LOPIT with differential
1041 ultracentrifugation for high-resolution spatial proteomics. Nat. Commun. 10, 331.
1042 https://doi.org/10.1038/s41467-018-08191-w
1043 Glembotski, C.C., 2007. Endoplasmic Reticulum Stress in the Heart. Circ. Res. 101, 975–984.
1044 https://doi.org/10.1161/CIRCRESAHA.107.161273
1045 Gonen, N., Meller, A., Sabath, N., Shalgi, R., 2019. Amino Acid Biosynthesis Regulation
1046 during Endoplasmic Reticulum Stress Is Coupled to Protein Expression Demands.
1047 iScience 19, 204–213. https://doi.org/10.1016/j.isci.2019.07.022
1048 Guan, B.-J., van Hoef, V., Jobava, R., Elroy-Stein, O., Valasek, L.S., Cargnello, M., Gao, X.-H.,
1049 Krokowski, D., Merrick, W.C., Kimball, S.R., Komar, A.A., Koromilas, A.E., Wynshaw-
1050 Boris, A., Topisirovic, I., Larsson, O., Hatzoglou, M., 2017. A Unique ISR Program
1051 Determines Cellular Responses to Chronic Stress. Mol. Cell 68, 885-900.e6.
1052 https://doi.org/10.1016/j.molcel.2017.11.007
1053 Hammond, D.E., Simpson, D.M., Franco, C., Wright Muelas, M., Waters, J., Ludwig, R.W.,
1054 Prescott, M.C., Hurst, J.L., Beynon, R.J., Lau, E., 2022. Harmonizing Labeling and
1055 Analytical Strategies to Obtain Protein Turnover Rates in Intact Adult Animals. Mol.
1056 Cell. Proteomics 21, 100252. https://doi.org/10.1016/j.mcpro.2022.100252
1057 Hanafusa, K., Wada, I., Hosokawa, N., 2019. SDF2-like protein 1 (SDF2L1) regulates the
1058 endoplasmic reticulum localization and chaperone activity of ERdj3 protein. J. Biol.
1059 Chem. 294, 19335–19348. https://doi.org/10.1074/jbc.RA119.009603
1060 Harding, H.P., Zhang, Y., Zeng, H., Novoa, I., Lu, P.D., Calfon, M., Sadri, N., Yun, C., Popko, B.,

1061 Paules, R., Stojdl, D.F., Bell, J.C., Hettmann, T., Leiden, J.M., Ron, D., 2003. An
1062 Integrated Stress Response Regulates Amino Acid Metabolism and Resistance to
1063 Oxidative Stress. Mol. Cell 11, 619–633. https://doi.org/10.1016/S1097-2765(03)00105-9
1064 Hetz, C., Zhang, K., Kaufman, R.J., 2020. Mechanisms, regulation and functions of the
1065 unfolded protein response. Nat. Rev. Mol. Cell Biol. 21, 421–438.
1066 https://doi.org/10.1038/s41580-020-0250-z
1067 Higuchi-Sanabria, R., Shen, K., Kelet, N., Frankino, P.A., Durieux, J., Bar-Ziv, R., Sing, C.N.,
1068 Garcia, E.J., Homentcovschi, S., Sanchez, M., Wu, R., Tronnes, S.U., Joe, L., Webster,
1069 B., Ahilon-Jeronimo, A., Monshietehadi, S., Dallarda, S., Pender, C., Pon, L.A., Zoncu,
1070 R., Dillin, A., 2020. Lysosomal recycling of amino acids affects ER quality control. Sci.
1071 Adv. 6, eaaz9805. https://doi.org/10.1126/sciadv.aaz9805
1072 Hulstaert, N., Shofstahl, J., Sachsenberg, T., Walzer, M., Barsnes, H., Martens, L., Perez-
1073 Riverol, Y., 2020. ThermoRawFileParser: Modular, Scalable, and Cross-Platform RAW
1074 File Conversion. J. Proteome Res. 19, 537–542.
1075 https://doi.org/10.1021/acs.jproteome.9b00328
1076 IBM Watson Health, 2023. Micromedex (Electronic Version).
1077 Jan, C.H., Williams, C.C., Weissman, J.S., 2014. Principles of ER cotranslational translocation
1078 revealed by proximity-specific ribosome profiling. Science 346, 1257521.
1079 https://doi.org/10.1126/science.1257521
1080 Kennedy, M.A., Hofstadter, W.A., Cristea, I.M., 2020. TRANSPIRE: A Computational Pipeline
1081 to Elucidate Intracellular Protein Movements from Spatial Proteomics Data Sets. J.
1082 Am. Soc. Mass Spectrom. 31, 1422–1439. https://doi.org/10.1021/jasms.0c00033
1083 Lakkaraju, A.K.K., Mary, C., Scherrer, A., Johnson, A.E., Strub, K., 2008. SRP Keeps
1084 Polypeptides Translocation-Competent by Slowing Translation to Match Limiting ER-
1085 Targeting Sites. Cell 133, 440–451. https://doi.org/10.1016/j.cell.2008.02.049
1086 Lam, M.P.Y., Wang, D., Lau, E., Liem, D.A., Kim, A.K., Ng, D.C.M., Liang, X., Bleakley, B.J.,
1087 Liu, C., Tabaraki, J.D., Cadeiras, M., Wang, Y., Deng, M.C., Ping, P., 2014. Protein
1088 kinetic signatures of the remodeling heart following isoproterenol stimulation. J. Clin.
1089 Invest. 124, 1734–1744. https://doi.org/10.1172/JCI73787
1090 Larance, M., Ahmad, Y., Kirkwood, K.J., Ly, T., Lamond, A.I., 2013. Global Subcellular
1091 Characterization of Protein Degradation Using Quantitative Proteomics. Mol. Cell.
1092 Proteomics 12, 638–650. https://doi.org/10.1074/mcp.M112.024547
1093 Lau, E., Cao, Q., Lam, M.P.Y., Wang, J., Ng, D.C.M., Bleakley, B.J., Lee, J.M., Liem, D.A.,
1094 Wang, D., Hermjakob, H., Ping, P., 2018. Integrated omics dissection of proteome
1095 dynamics during cardiac remodeling. Nat. Commun. 9, 120.
1096 https://doi.org/10.1038/s41467-017-02467-3
1097 Lee, J.W., Koeppen, M., Seo, S.-W., Bowser, J.L., Yuan, X., Li, J., Sibilia, M., Ambardekar,
1098 A.V., Zhang, X., Eckle, T., Yoo, S.-H., Eltzschig, H.K., 2020. Transcription-independent
1099 Induction of ERBB1 through Hypoxia-inducible Factor 2A Provides Cardioprotection
1100 during Ischemia and Reperfusion. Anesthesiology 132, 763–780.
1101 https://doi.org/10.1097/ALN.0000000000003037
1102 Lemberg, M.K., Strisovsky, K., 2021. Maintenance of organellar protein homeostasis by ER-
1103 associated degradation and related mechanisms. Mol. Cell 81, 2507–2519.
1104 https://doi.org/10.1016/j.molcel.2021.05.004
1105 Liu, C., Li, X., Li, C., Zhang, Z., Gao, X., Jia, Z., Chen, H., Jia, Q., Zhao, X., Liu, J., Liu, B., Xu,
1106 Z., Tian, Y., He, K., 2018. SLC3A2 is a novel endoplasmic reticulum stress-related
1107 signaling protein that regulates the unfolded protein response and apoptosis. PloS
1108 One 13, e0208993. https://doi.org/10.1371/journal.pone.0208993
1109 Liu, C.-L., Li, X., Hu, G.-L., Li, R.-J., He, Y.-Y., Zhong, W., Li, S., He, K.-L., Wang, L.-L., 2012.
1110 Salubrinal protects against tunicamycin and hypoxia induced cardiomyocyte

apoptosis via the PERK-eIF2 signaling pathway. J. Geriatr. Cardiol. JGC 9, 258–268. https://doi.org/10.3724/SP.J.1263.2012.02292

Maas, R.G.C., Lee, S., Harakalova, M., Snijders Blok, C.J.B., Goodyer, W.R., Hjortnaes, J., Doevendans, P.A.F.M., Van Laake, L.W., van der Velden, J., Asselbergs, F.W., Wu, J.C., Sluijter, J.P.G., Wu, S.M., Buikema, J.W., 2021. Massive expansion and cryopreservation of functional human induced pluripotent stem cell-derived cardiomyocytes. STAR Protoc. 2, 100334. https://doi.org/10.1016/j.xpro.2021.100334

Mårtensson, C.U., Priesnitz, C., Song, J., Ellenrieder, L., Doan, K.N., Boos, F., Floerchinger, A., Zufall, N., Oeljeklaus, S., Warscheid, B., Becker, T., 2019. Mitochondrial protein translocation-associated degradation. Nature 569, 679–683. https://doi.org/10.1038/s41586-019-1227-y

Martin, T.G., Myers, V.D., Dubey, P., Dubey, S., Perez, E., Moravec, C.S., Willis, M.S., Feldman, A.M., Kirk, J.A., 2021a. Cardiomyocyte contractile impairment in heart failure results from reduced BAG3-mediated sarcomeric protein turnover. Nat. Commun. 12, 2942. https://doi.org/10.1038/s41467-021-23272-z

Martin, T.G., Tawfik, S., Moravec, C.S., Pak, T.R., Kirk, J.A., 2021b. BAG3 expression and sarcomere localization in the human heart are linked to HSF-1 and are differentially affected by sex and disease. Am. J. Physiol.-Heart Circ. Physiol. 320, H2339–H2350. https://doi.org/10.1152/ajpheart.00419.2020

Martínez-Martínez, E., Ibarrola, J., Fernández-Celis, A., Santamaria, E., Fernández-Irigoyen, J., Rossignol, P., Jaisser, F., López-Andrés, N., 2017. Differential Proteomics Identifies Reticulocalbin-3 as a Novel Negative Mediator of Collagen Production in Human Cardiac Fibroblasts. Sci. Rep. 7, 12192. https://doi.org/10.1038/s41598-017-12305-7

McDowell, G.S., Gaun, A., Steen, H., 2013. iFASP: combining isobaric mass tagging with filter-aided sample preparation. J. Proteome Res. 12, 3809–3812. https://doi.org/10.1021/pr400032m

Meiners, S., Heyken, D., Weller, A., Ludwig, A., Stangl, K., Kloetzel, P.-M., Krüger, E., 2003. Inhibition of Proteasome Activity Induces Concerted Expression of Proteasome Genes and de Novo Formation of Mammalian Proteasomes. J. Biol. Chem. 278, 21517–21525. https://doi.org/10.1074/jbc.M301032200

Mulvey, C.M., Breckels, L.M., Crook, O.M., Sanders, D.J., Ribeiro, A.L.R., Geladaki, A., Christoforou, A., Britovšek, N.K., Hurrell, T., Deery, M.J., Gatto, L., Smith, A.M., Lilley, K.S., 2021. Spatiotemporal proteomic profiling of the pro-inflammatory response to lipopolysaccharide in the THP-1 human leukaemia cell line. Nat. Commun. 12, 5773. https://doi.org/10.1038/s41467-021-26000-9

Orre, L.M., Vesterlund, M., Pan, Y., Arslan, T., Zhu, Y., Fernandez Woodbridge, A., Frings, O., Fredlund, E., Lehtiö, J., 2019. SubCellBarCode: Proteome-wide Mapping of Protein Localization and Relocalization. Mol. Cell 73, 166-182.e7. https://doi.org/10.1016/j.molcel.2018.11.035

Pakos-Zebrucka, K., Koryga, I., Mnich, K., Ljujic, M., Samali, A., Gorman, A.M., 2016. The integrated stress response. EMBO Rep. 17, 1374–1395. https://doi.org/10.15252/embr.201642195

Ren, J., Bi, Y., Sowers, J.R., Hetz, C., Zhang, Y., 2021. Endoplasmic reticulum stress and unfolded protein response in cardiovascular diseases. Nat. Rev. Cardiol. 18, 499–521. https://doi.org/10.1038/s41569-021-00511-w

Sayers, E.W., Bolton, E.E., Brister, J.R., Canese, K., Chan, J., Comeau, D.C., Connor, R., Funk, K., Kelly, C., Kim, S., Madej, T., Marchler-Bauer, A., Lanczycki, C., Lathrop, S., Lu, Z., Thibaud-Nissen, F., Murphy, T., Phan, L., Skripchenko, Y., Tse, T., Wang, J., Williams, R., Trawick, B.W., Pruitt, K.D., Sherry, S.T., 2022. Database resources of the national center for biotechnology information. Nucleic Acids Res. 50, D20–D26.

1161 https://doi.org/10.1093/nar/gkab1112
1162 Schwanhäusser, B., Busse, D., Li, N., Dittmar, G., Schuchhardt, J., Wolf, J., Chen, W., Selbach,
1163 M., 2011. Global quantification of mammalian gene expression control. Nature 473,
1164 337–342. https://doi.org/10.1038/nature10098
1165 Shin, J.J.H., Crook, O.M., Borgeaud, A.C., Cattin-Ortolá, J., Peak-Chew, S.Y., Breckels, L.M.,
1166 Gillingham, A.K., Chadwick, J., Lilley, K.S., Munro, S., 2020. Spatial proteomics defines
1167 the content of trafficking vesicles captured by golgin tethers. Nat. Commun. 11, 5987.
1168 https://doi.org/10.1038/s41467-020-19840-4
1169 Tan, X., Lambert, P.F., Rapraeger, A.C., Anderson, R.A., 2016. Stress-Induced EGFR
1170 Trafficking: Mechanisms, Functions, and Therapeutic Implications. Trends Cell Biol.
1171 26, 352–366. https://doi.org/10.1016/j.tcb.2015.12.006
1172 Tan, X., Thapa, N., Sun, Y., Anderson, R.A., 2015. A Kinase-Independent Role for EGF
1173 Receptor in Autophagy Initiation. Cell 160, 145–160.
1174 https://doi.org/10.1016/j.cell.2014.12.006
1175 The, M., MacCoss, M.J., Noble, W.S., Käll, L., 2016. Fast and Accurate Protein False Discovery
1176 Rates on Large-Scale Proteomics Data Sets with Percolator 3.0. J. Am. Soc. Mass
1177 Spectrom. 27, 1719–1727. https://doi.org/10.1007/s13361-016-1460-7
1178 Toro, R., Pérez-Serra, A., Mangas, A., Campuzano, O., Sarquella-Brugada, G., Quezada-Feijoo,
1179 M., Ramos, M., Alcalá, M., Carrera, E., García-Padilla, C., Franco, D., Bonet, F., 2022.
1180 miR-16-5p Suppression Protects Human Cardiomyocytes against Endoplasmic
1181 Reticulum and Oxidative Stress-Induced Injury. Int. J. Mol. Sci. 23, 1036.
1182 https://doi.org/10.3390/ijms23031036
1183 Tsai, P.-L., Cameron, C.J.F., Forni, M.F., Wasko, R.R., Naughton, B.S., Horsley, V., Gerstein,
1184 M.B., Schlieker, C., 2022. Dynamic quality control machinery that operates across
1185 compartmental borders mediates the degradation of mammalian nuclear membrane
1186 proteins. Cell Rep. 41, 111675. https://doi.org/10.1016/j.celrep.2022.111675
1187 Ustrell, V., Hoffman, L., Pratt, G., Rechsteiner, M., 2002. PA200, a nuclear proteasome
1188 activator involved in DNA repair. EMBO J. 21, 3516–3525.
1189 https://doi.org/10.1093/emboj/cdf333
1190 Villanueva, E., Smith, T., Pizzinga, M., Elzek, M., Queiroz, R.M.L., Harvey, R.F., Breckels, L.M.,
1191 Crook, O.M., Monti, M., Dezi, V., Willis, A.E., Lilley, K.S., 2022. A system-wide
1192 quantitative map of RNA and protein subcellular localisation dynamics (preprint). Cell
1193 Biology. https://doi.org/10.1101/2022.01.24.477541
1194 Vonk, L.A., Doulabi, B.Z., Huang, C.-L., Helder, M.N., Everts, V., Bank, R.A., 2010.
1195 Endoplasmic reticulum stress inhibits collagen synthesis independent of collagen-
1196 modifying enzymes in different chondrocyte populations and dermal fibroblasts.
1197 Biochem. Cell Biol. Biochim. Biol. Cell. 88, 539–552. https://doi.org/10.1139/o09-174
1198 Xie, Y., Varshavsky, A., 2001. RPN4 is a ligand, substrate, and transcriptional regulator of the
1199 26S proteasome: a negative feedback circuit. Proc. Natl. Acad. Sci. U. S. A. 98, 3056–
1200 3061. https://doi.org/10.1073/pnas.071022298
1201 Xu, H., Ju, D., Jarois, T., Xie, Y., 2008. Diminished feedback regulation of proteasome
1202 expression and resistance to proteasome inhibitors in breast cancer cells. Breast
1203 Cancer Res. Treat. 107, 267–274. https://doi.org/10.1007/s10549-007-9553-4